University of Stavanger

Faculty of Science and Technology

MASTER'S THESIS

Study program/ Specialization: Petroleum Engineering/Reservoir Technology	Spring semester, 2014 Open
Writer: Thomas Melvin Danielsen	…… (Writer's signature)
Faculty supervisor: Steinar Evje	
Thesis title: A mathematical model for spontaneous imbibition as a recovery mechanism	
Credits (ECTS): 30	
Key words: Spontaneous imbibition Analytical solution Wettability Numerical modelling	Pages: 79 + enclosure: 2 Stavanger, 04/06/2014 Date/year

A Mathematical Model for Spontaneous Imbibition as a Recovery Mechanism

Master Thesis by Thomas Melvin Danielsen

University of Stavanger

Spring 2014

Acknowledgments

This thesis was written in the spring of 2014 as a requirement for the degree of Master of Science in Petroleum Technology at the University of Stavanger.

I would like to express my gratitude to my thesis advisor Steinar Evje for his excellent guidance, support and patience throughout the process. Writing the thesis has been an exiting experience and I have gained a lot of knowledge and insight into processes that were less known to me before. In regards to software I have had an introduction into both LaTeX and MATLAB. In the process of creating scripts for solving the models in MATLAB, Steinars inputs has been invaluable.

I would also like to thank my family for their support throughout the process and for always believing in me. A special thanks to my wife Maren and my daughter Melvina for being so patient with me. It has been a busy period combining a full-time job with the writing of the thesis. I would not have managed if it weren't for your encouragement. And also a thank you to my friend and classmate Eirik for proofreading the thesis.

Abstract

Spontaneous imbibition is a process where the wetting fluid displaces the non-wetting fluid in a porous medium by means of capillary forces. Spontaneous imbibition plays a significant role in the recovery of hydrocarbons, especially from fractured reservoirs and particularly where the matrix has low permeability. An increasing portion of remaining reserves in both oil and gas reservoirs are retained in low permebility rocks and in these reservoirs spontaneous imbibition is the key recovery mechanism. In this study we have derived an analytical solution of a model that describes counter-current imbibition, in terms of a non-linear diffusion equation, based on ideas presented in a paper by Tavassoli, Zimmerman and Blunt [19]. We have also considered a discrete scheme for the equation which allowed us to compute a numerical solution of the model. We have then used the solutions to gain insight into which parameters that control the oil recovery by spontaneous imbibition. A comparison of the numerical and the analytical solution have been made to test the validity of the analytical solution.

Contents

1. Introduction

In this thesis we will study spontaneous imbibition, a process where the wetting fluid, by means of capillary forces, will displace the non-wetting fluid. Spontanous imbibition is an important recovery mechanism in fractured reservoirs [4], and it is also strongly dependent on wettability, a property that can be altered through EOR mechanisms [20]. The focus point of this study will be a paper by Tavassoli et al. [19]. They present an analytical solution to a model for oil recovery during counter-current spontaneous imbibition in water-wet systems. A thorough description of the objectives is presented in sec. 1.3.

The thesis will be divided into 4 parts. In the first part, consistiting of chapter 1 and chapter 2, we will describe the objectives and take a look at the fundamental concepts relevant to this thesis, in the second part, consisting of chapter 3, we will attempt to reproduce the model that Tavassoli et al. proposed [19], including the solution procedure for early and late times. In the third part, consisiting of chapter 4, we will focus on solving the model both analytically and numerically, and also look at the model's dependence on specific parameters. In the last part, consisting of chapter 5 and chapter 6, we will compare the analytical and numerical models and conclude.

1.1. Enhanced oil recovery

Oil recovery operations can usually be divided into three stages: The primary production period, which is the production resulting from the initial pressure naturally existing in the reservoir. The secondary production period, which is the use of mechanical energy to maintain pressure in the reservoir, usually by water or gas injection. The tertiary oil recovery methods, which are also referred to as enhanced oil recovery [7]. The target of EOR methods is to recover the oil not produced by the conventional primary and secondary production methods, usually by use of injectants to decrease residual oil and increase volumetric sweep [7][16].

Thermal recovery by steam injection through imbibition of condensed water, water-flooding of heterogenous reservoirs as well as alternating injection of water and gas are all different types of secondary recovery processes where the important role of spontaneous imbibition has been recognized. [13]. As mentioned in the next section the recovery of oil by spontaneous imbibition of brine into reservoir rock is of special importance in fractured reservoirs. EOR processes in fractured reservoirs must try

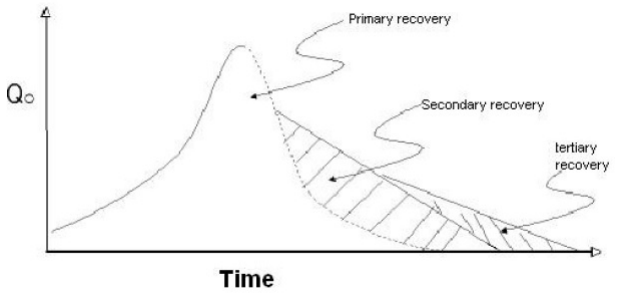

Figure 1.1.: Oil production vs. time for different production methods. Figure from [9]

to improve the spontaneous imbibition process. The most common EOR method to improve the spontaneous imbibition process is wettability alteration. Many carbonate reservoirs act as neutral or preferentially oil-wet [20], and for oil-wet reservoirs no spontaneous imbibition of water takes place. However, if the injected fluid can alter the wetting condition towards a more water-wet state, improvement of oil recovery is possible [20]. For carbonate reservoirs the use of cationic surfactants have been used to alter the wettability to more water-wet conditions, especially through the ion-pair interaction between the cationic surfactants and the carboxylates in crude oil, which are the most strongly adsorbed material onto the chalk surface [18]. When flooding the reservoir with seawater, the potential determining ions Ca^{2+} and SO_4^{2+} present have also been shown to greatly influence the surface charge of chalk and thereby modify the wettability during the water injection [20]. In addition Mg^{2+} have also been found to be a strong potential determining ion [20].

1.2. Fractured reservoirs

Naturally fractured reservoirs are important oil and gas resources [4]. The reservoirs are composed of two parts, a low permeability matrix block, surrounded by fractures with much higher permeability. Most of the recoverable oil is located in the low permeability matrix. Waterflooding is frequently implemented to increase recovery in fractured reservoirs [4]. However, the success of the waterflood is largely determined by the ability of the matrix block to imbibe the injected water and push the oil out in the highly mobile fracture system and towards the production well. If the reservoir is oil-wet the water will not displace the oil in the matrix since there is no spontaneous imbibition of water, and only the oil in the fractures will be displaced. This will result in poor recoveries and early breakthrough of water. In cases where the fractured reservoir is water-wet, imbibition can lead to significant recoveries [4].

1.3. Objectives

In this thesis we focus on a mathematical model for spontaneous imbibition. We restrict ourselves to the case with a fixed wetting case, i.e no alteration of wettability occurs. As mentioned the starting point for this thesis is a paper presented by Tavassoli et al. [19]. They present an analytical solution of the model that describes counter-current imbibition in terms of a nonlinear diffusion equation. The objective of the thesis is to reproduce this analytical solution and fill in some details in the derivation of the model, we then implement MATLAB code to visualize this solution and its dependence on various parameters. We make several observations of the characteristic behaviour of the model based on the analytical approach. The analytical approach involves several assumptions and simplifications when an early and a late time solution is derived. Hence it is instructive to assess the consequences of these assumptions. We also consider a discrete scheme for the model. The analytical solution will then be compared to the approximate solution obtained by solving the diffusion equation numerically. We will also include some comparison with experimental data.

2. Fundamentals

In this chapter we will describe general principles and fundamental concepts related to this thesis.

2.1. Interfacial tension

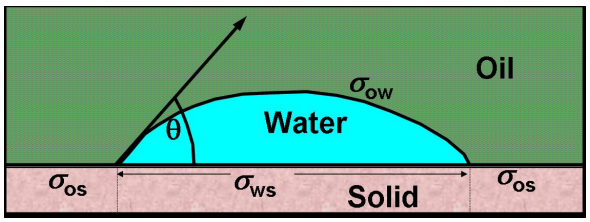

Figure 2.1.: Interfacial forces at an interface between two immiscble fluids and a solid. Figure from [5].

Interfacial tension is a term describing the acting forces between two immiscible fluids in contact with each other. One can view the interfacial tension as the force required per unit length to extend the surface one unit [7]. When the immiscible fluids are located in a porous medium the interfacial tension influences the saturations, distributions and displacements of the fluids [7], and is thus an important parameter in many recovery methods. The interfacial tension is denoted by σ, and when in a pressure equilibrium state, the magnitude of interfacial tension describes how much energy is required to keep the two fluids separated [23]. Fig. 2.1 shows the interfacial forces between two immiscible fluids, oil and water in this case, denoted by σ_{ow}.

2.2. Wettability

The tendency of a fluid to adhere to a solid surface if another fluid is present is called the wettability. When there are two or more immiscible fluids present in a system, one of them will usually be more attracted to the solid than the other [7]. The fluid that is more strongly attracted is called the wetting fluid, e.g if water is more attracted to the solid we call it the wetting phase and we say the rock is water-wet [1][7]. Referring to Fig. 2.2 we can say, although very simplified, that if the

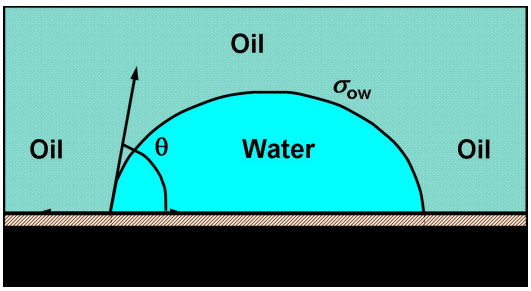

Figure 2.2.: Figure showing a water drop on a solid surrounded by oil. θ is the contact angle between the oil/water/solid interface measured trough the water phase, and σ_{ow} is the interfacial tension between oil and water. Figure from [5].

wetting angle, θ, is between 0° and 90° the solid is water-wet, and from 90° to 180° it is characterized as oil-wet. Tab. 2.1 shows a more comprehensive classification of different wetting states as a function of wetting angle.

Wetting angle (degree)	Wettability preference
0 - 30	Strongly water-wet
30 - 90	Preferentially water-wet
90	Neutral wettability
90 - 150	Preferentially oil-wet
150 - 180	Strongly oil-wet

Table 2.1.: Arbitrary wettability classes for water-oil system. Table from [23].

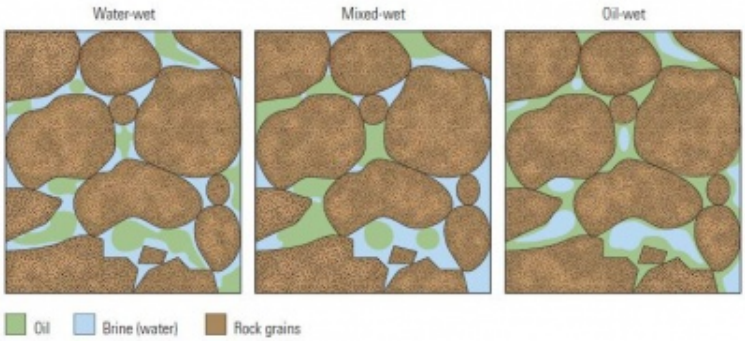

Figure 2.3.: Wetting in pores. In a water-wet case (left), oil remains in the center of the pores. The reverse condition holds if all surfaces are oil-wet (right). In the mixed-wet case, oil has displaced water from some of the surfaces but is still in the centers of the water-wet curves (middle). The three conditions shown have similar saturations of water and oil [1]. Figure from [1].

Rock wettabilities has a strong influence on the nature of fluid saturations and also the relative permeability characteristics of a fluid/rock system as can be seen in

Fig. 2.4. The location of a phase within the pore structure depends on the wettability of that phase, as we see in figure Fig. 2.3. For water-wet systems the oil is trapped in the pores while the water is spread over the surface of the rock, and inversely for oil-wet systems [7]. Mixed-wet systems are more complex, where we may encounter both oil- and water-wet areas in the same reservoir. This is usually a result of heterogenities in chemical composition of the rock surface, the rocks mineral composistion or a difference in saturation history [1]. There also exists intermediate wettability where the wetting systems have little to no preference between oil and water. In this thesis the focus has mainly been strongly water-wet systems.

2.3. Relative permeability

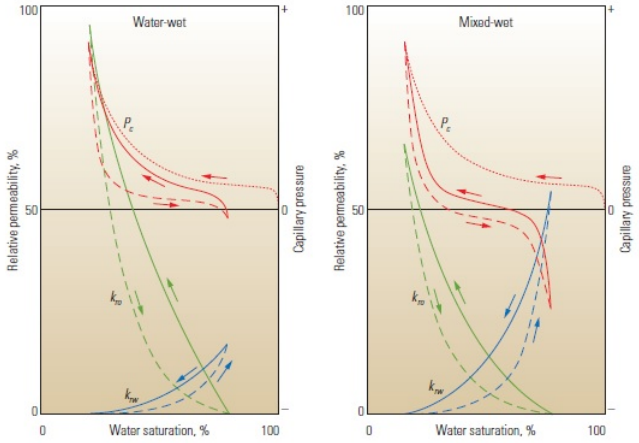

Figure 2.4.: Relative permeability curves in water- and mixed-wet reservoirs. This figure also contains capillary pressure curves which will not be discussed in this section. Figure from [1].

Relative permeability is the relationship between absolute and effective permeability in a porous system and is defined as:

$$K_{rl} = \frac{K_e}{K} \tag{2.1}$$

where K_{rl} is the relative permeability, K is the absolute permeability, that is, when the system is 100% saturated by a single fluid and K_e is the effective permeability (the permeability of a given fluid when more than one fluid is present) of a particular fluid in the system [23]. From Eq.(2.1) we see that relative permeability is the ratio of the effective permeability to the absolute permeability. In short we can say that it is a measure of how easily a fluid can pass through a porous medium in the presence

of another fluid, and it is a strong function of the respective phase saturations. Relative permeability is a rock-fluid property, so the functionality between relative permeability and saturations will also be a function of rock properties like pore size distribution and wettability [23]. Generally there is not a strong correlation between relative permeability and fluid properties, though when there is a drastic change in certain properties, like interfacial tension, the relative permeability can be affected [7][23]. Fig. 2.4 illustrates the difference in relative permeability curves for different wetting conditions. At low water saturations the K_{ro} values are lower in the mixed-wet case because the oil is in competition with the water in the large pores. Similarly, in the water-wet case the K_{rw} is reduced at high water saturation because the large pores is preferentially occupied by oil [1].

2.3.1. Corey relative permeability

In this thesis we have used the Corey relative permeability correlation for oil and water, which are given by:

$$K_{ro} = K_{ro}^{max}(1-S)^b, \qquad K_{rw} = K_{rw}^{max}(S)^a \tag{2.2}$$

where K_{ro}^{max} and K_{rw}^{max} is introduced as the end point relative permeabilities of oil and water respectively, S is the normalized water saturation from Eq.(2.11), b is the Corey oil exponent and a is the Corey water exponent. Fig. 2.5 shows a set of relative permeability curves created using the Corey relative permeability correlation. Based on the high intitial K_{ro} and the reduced K_{rw} we see that these relative permeability curves are for water-wet reservoirs.

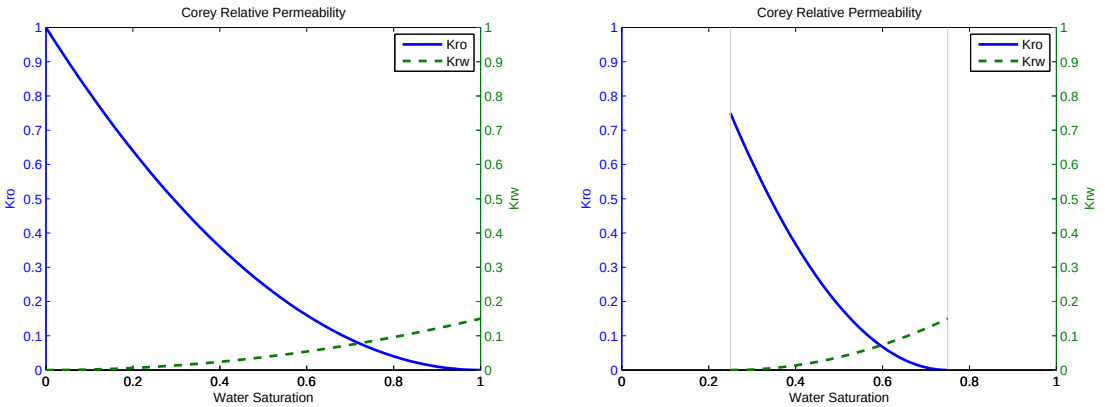

(a) Relative permeability vs. normalized water saturation **(b)** Relative permeability vs. water saturation

Figure 2.5.: Figure showing a set of Corey relative permeability curves.

2.4. Capillary pressure

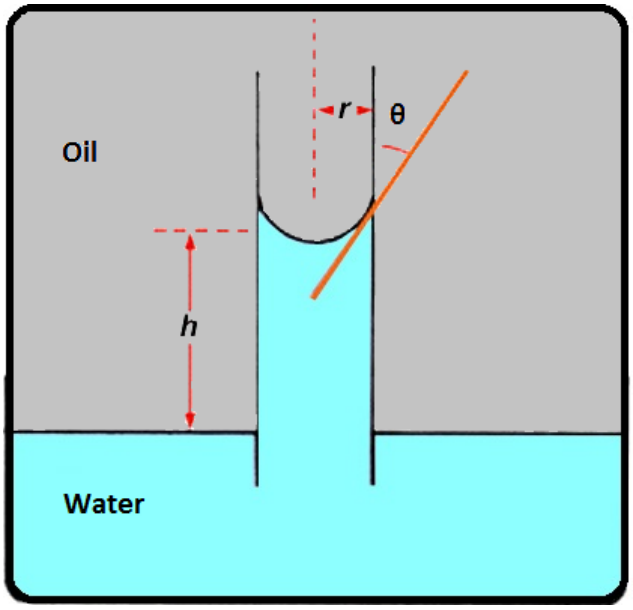

Figure 2.6.: Illustration of a capillary tube experiment.

Whenever immiscible fluids are in contact with each other there exists a molecular pressure difference across the interface of the fluids. This pressure difference is what is defined as the capillary pressure [23]. In short, Ursin and Zolotukhin describes the capillary pressure as the molecular pressure difference between the wetting and the non wetting fluid [23].

$$P_c = P_{non-wetting\,phase} - P_{wetting\,phase} \tag{2.3}$$

The fluid rise in a capillary tube is one way of illustrating the capillary pressure (Fig. 2.6). The fluid above the water is oil and since the glass has a preference for water, there will be a capillary rise in the tube. It can be shown that the capillary pressure in a tube is given by

$$P_c = \frac{2\sigma_{ow} cos\theta}{r} \tag{2.4}$$

Through the relation in Eq.(2.4) we see that the capillary pressure is related to the interfacial tension between the fluids (σ_{ow}), the wettability of the fluids (through the contact angle θ), and the size of the capillary, r. Because of the complexity of the porous media, the capillary tube model is often used as an idealized approximation to capillary phenomenon in oil bearing rocks [7]. Despite the idealization

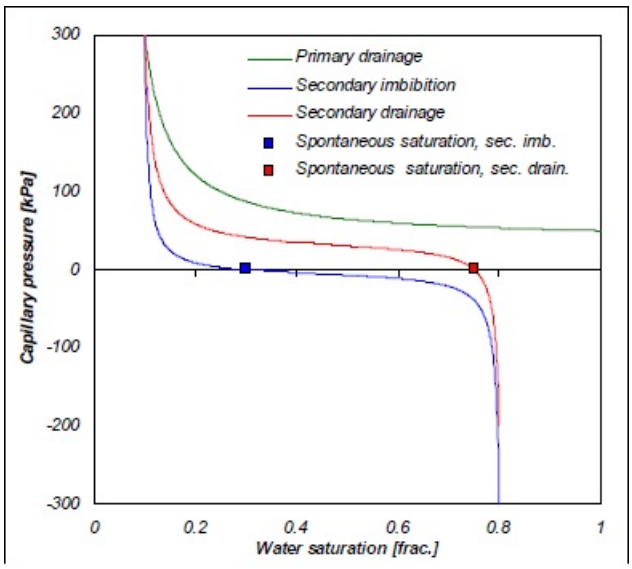

Figure 2.7.: Basic capillary pressure curves. Figure from [11]

the experiment can still be related to fluid contacts and saturation distributions in a reservoir [7][23].

Fig. 2.7 shows a set of basic capillary pressure curves. *Drainage* refers to a decrease in the wetting fluid saturation and *imbibition* refers to an increase in the wetting fluid saturation [23]. So for a reservoir originally filled with water, the primary drainage curve corresponds to the initial filling of the reservoir with oil. The secondary drainage curve relates to later displacement processes and the imbibition curve relates to the displacement of oil by water.

Referring to Fig. 2.8 we see capillary pressure function for both water- and mixed-wet reservoirs. The capillary pressure curve stays positive over most of the saturation range in the strongly water-wet case, this is because all of the surface imbibe water. In the mixed-wet case its sign has both positive and negative portions, which signifies that some parts of the surface imbibe water and others imbibe oil [1].

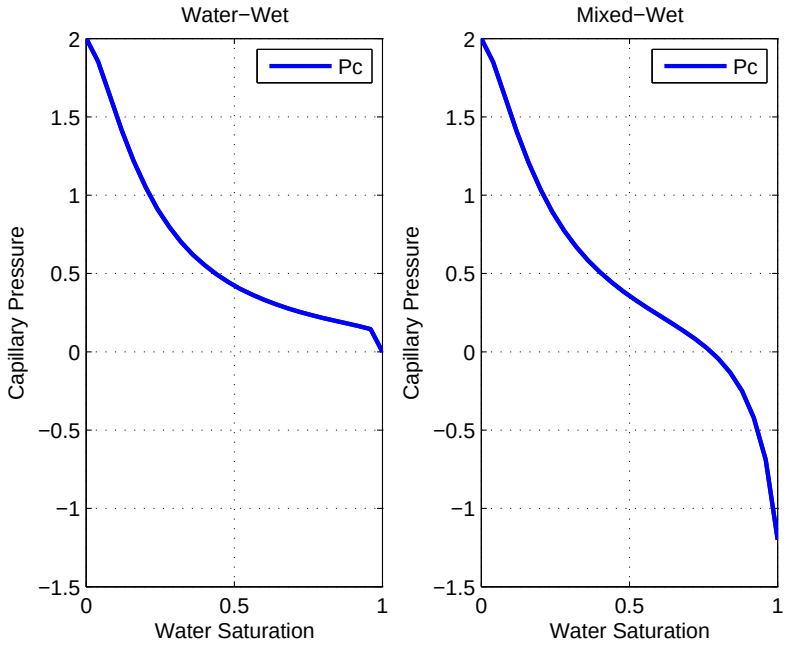

Figure 2.8.: Figure showing capillary pressure functions for water- and mixed-wet states. The figure was created using LET capillary pressure described in sec. 2.4.2

2.4.1. Leverett J-function

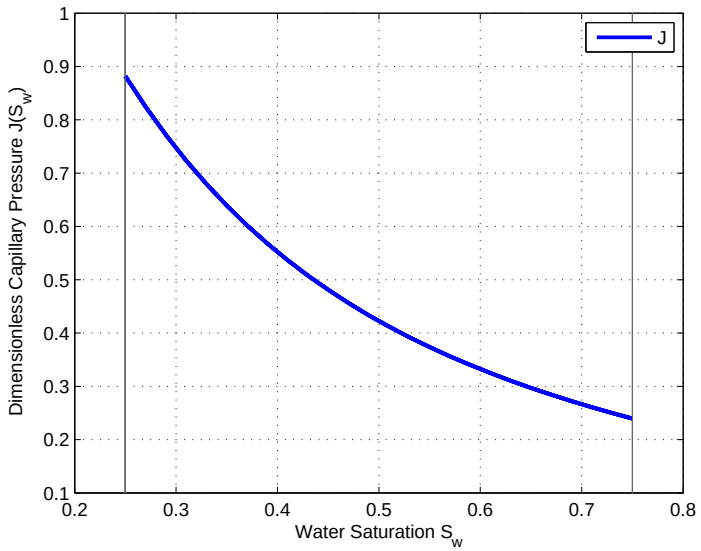

Figure 2.9.: Figure showing dimensionless capillary pressure, the Leverett J-function, vs. water saturation S_w.

The Leverett J-function is a dimensionless capillary pressure function of water satu-

ration. It is used to eliminate capillary pressure differences beween different strata, and to describe reservoirs of similar lithology [8]. The Leverett J-function can be expressed by the formula:

$$J(S_w) = \frac{P_c}{\sigma}\sqrt{\frac{K}{\phi}} \tag{2.5}$$

where P_c is the capillary pressure, σ is the interfacial tension, K is the permeability and ϕ the porosity. The physical interpretation of the Leverett J-function is that for reservoirs whose lithology is similar and have fixed saturations, the J-function remains unaltered. Differences caused by different media or fluids can also be eliminated by the J-function [8]. Fig. 2.9 shows a J-function where the P_c curve was created using LET-Capillary pressure as described in the next section.

2.4.2. LET capillary pressure

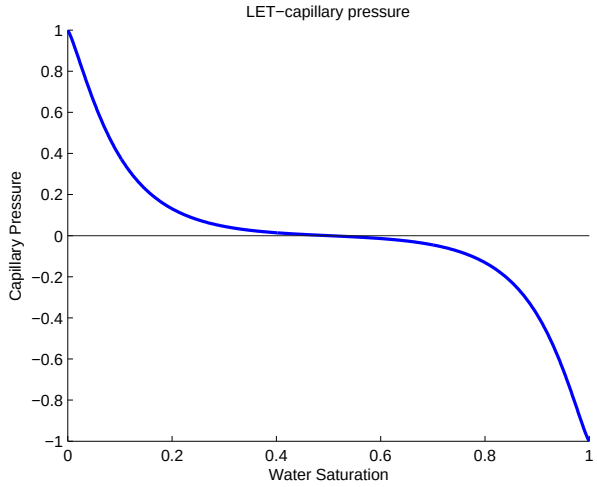

Figure 2.10.: Example of capillary pressure curve created using the LET capillary pressure correlation.

Lomeland et al. proposed a new analytical correlation for the capillary pressure function in 2008 [11]. The advantage of the LET model is that it has a greater degree of flexibility than previously proposed capillary pressure correlations.

The LET type correlation for imbibition is given by:

$$P_C = \frac{P_C^{si}(1 - S_{wn})^{L^{si}}}{(1 - S_{wn})^{L^{si}} + E^{si}S_{wn}^{T^{si}}} + \frac{P_C^{si}S_{wn}^{L^{fi}}}{S_{wn}^{L^{fi}} + E^{fi}(1 - S_{wn})^{T^{fi}}} \tag{2.6}$$

where the parameter L describes the lower part of the curve. The parameter T describes the top part of the curve in much the same way that the L-parameter describes the lower part, and the parameter E describes the position of the slope of the curve. Increasing the value of the E-parameter shifts the slope towards the high end of the curve and opposite for decreasing values of the E-parameter [11]. The first term in Eq.(2.6) describes the positive part of the curve, which is the spontaneous imbibition, denoted by the superscript si, and the second term describes the negative, forced part of the curve, denoted by the superscript fi. Fig. 2.10 shows an example of an arbitrary capillary pressure curve created using LET, and Fig. 2.11 shows the flexibility of LET capillary pressure for the spontaneous imbibition part of the curve.

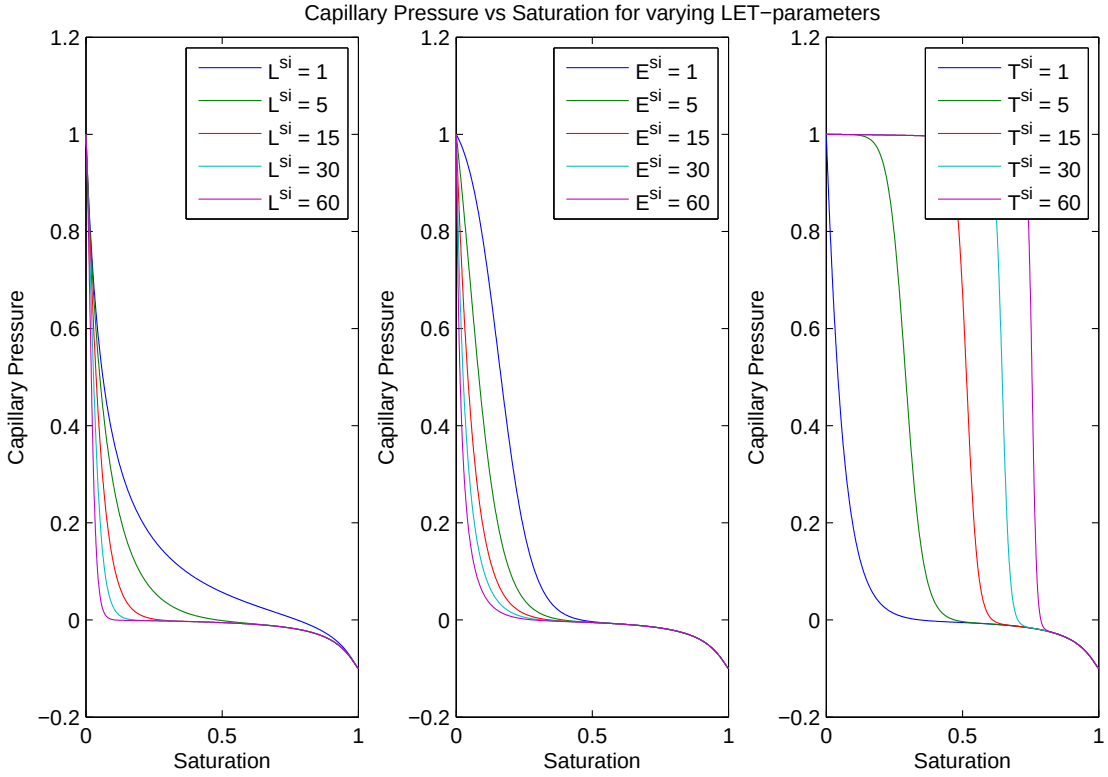

Figure 2.11.: Figure showing capillary pressure curves with varying LET-parameters for the spontaneous imbibition curve.

Since no experimental data has been given for the capillary pressure, the flexibility of the LET capillary pressure has made it easier constructing capillary pressure curves that corresponds to the J-function used by Tavassoli with a gradient of 0.19 for S=1.

2.5. Spontaneous imbibition

Spontaneous imbibition occurs when the wetting phase spontaneously displaces the non-wetting phase in a porous medium. The mechanism is regarded as one of the most important contributors to increase displacement efficiency in fractured reservoirs [16]. Imbibition can take place by two types of flow, co-current and counter-current [4]. In co-current flow the water and oil flows in the same direction, and the water expels the oil from the matrix. For counter-current imbibition the oil and water flow in opposite directions and the oil flows back along the same path that water has imbibed. Even though co-current imbibition can be faster and more efficient, mainly due to flow patterns and more viscous friction as the two phases pass eachother [22], counter-current imbibition will often be the only mechanism possible. Particularly in fractured reservoirs where the lower permeability matrix may be surrounded by water as mentioned in section sec. 1.2. In this thesis we will only study counter-current imbibition.

Many attempts have been made to match the oil recovery by imbibition as a function of dimensionless time to a simple analytic expression. Zhang et al. [21] proposed the following equation, which is a simple exponential function of time, the expression matched a range of imbibition experiments on samples with different geometry and fluid properties [19].

$$R = R\infty(1 - e^{-\alpha t_{DE}}) \tag{2.7}$$

where R is recovery, $R\infty$ is ultimate recovery and t_{DE} is an empirical scaling equation for dimensionless time. The constant α is approximately 0.05 [19]. Equation 2.7 is based on two assumptions: (1) the recovery is a continous function of time and converges to a finite limit and; (2) none of the properties that determine the rate of convergence change during the process [17]. The dimensionless time in the expression was proposed by Ma et al. [12] and is defined by:

$$t_{DE} = t\sqrt{\frac{K}{\phi}}\frac{\sigma}{\sqrt{\mu_w\mu_o}}\frac{1}{L_c} \tag{2.8}$$

where σ is the interfacial tension and L_C is a characteristic or effective length given by:

$$L_C = \frac{V}{\sum_{i=1}^{n}\frac{A_i}{l_i}} \tag{2.9}$$

where V is matrix block volume, A_i is the area open to imbibition in the ith direction and l_i is the distance from the open surface to a no-flow boundary. The physical

interpretation of the characteristic length L_C is therefore to quantify the length a wetting front can travel without encountering a boundary or another imbibition front [12][14].

Equation (2.7) can be re-written in terms of the average water saturation in the core, $\bar{S}_w$:

$$\frac{R}{R\infty} = \frac{\bar{S}_w - S_{wi}}{1 - S_{or} - S_{wi}} \tag{2.10}$$

where S_{wi} is the initial water saturation and S_{or} is the residual oil saturation, or to be described more accurately, it is the oil saturation that is reached after spontaneous imbibition only. Defining a normalized saturation:

$$S = \frac{S_w - S_{wi}}{1 - S_{wi} - S_{or}}; \qquad 1 \geq S \geq 0. \tag{2.11}$$

$$\bar{S} = 1 - e^{-\alpha t_{DE}} \tag{2.12}$$

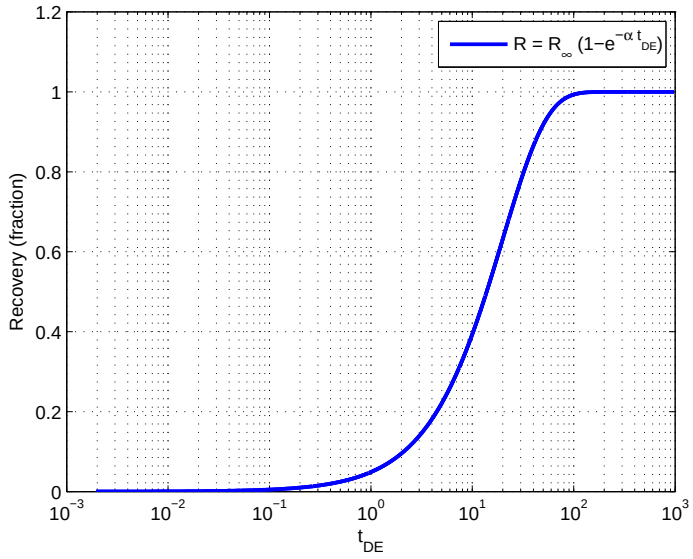

Figure 2.12.: Exponential empirical correlation, Eq.(2.7) as a function of dimensionless time t_{DE}, Eq.(2.8), without experimental data.

2.5.1. Scaling groups

Scaling groups are a tool used to describe how key parameters influence spontaneous imbibition, and they are essential whenever the process of spontaneous imbibition needs to be understood [14][15]. Schmid et al. lists some of the important features of scaling groups as: 1) being a constraint for an appropriate upscaling of laboratory data, 2) beeing of key importance when modelling and simulating flow in fractured and heterogenous reservoirs, and they are also 3) necessary when evaluating the feasibility of water injection in geothermal reservoirs [15]. Because of the vast importance of spontaneous imbibition and scaling models, a lot of research has been done on the subject. The scaling group has most commonly been expressed in the form of dimensionless time t_D. There are many conditions that apply to the scaling equation, including identical core sample shapes and fluid viscosities [12].

One of the most widely applied scaling equation was proposed by Mattax and Kyte in 1962. It is similar to the one proposed by Ma et al. [12] in this chapter, Eq.(2.8), but it did not include the viscosity of oil. Also, the characteristic lengh, L_C, in their equation did not correspond to any shape factor. The shape factor was proposed to compensate for the effects of shapes and boundary conditions, allowing more experimental data to be compared to the models. The expression we will derive in this thesis was proposed by Tavassoli et al. [19], and has been proven to match experiments well, although not as well as the scaling group wich includes the viscosity of water, Eq.(2.8).

2.5.2. Boundary conditions

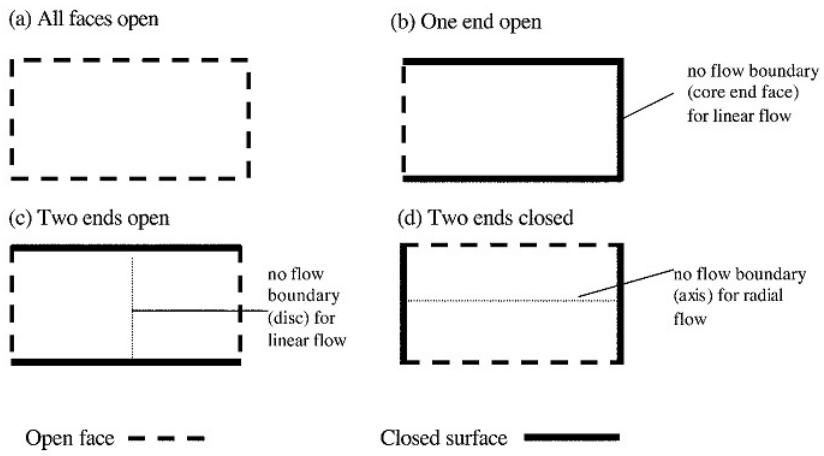

Figure 2.13.: Figure showing boundary conditions for core samples. Figure from [12].

The experiments used in the paper by Tavasolli et al. [19] where carried out by

Mattax and Kyte, Hamon and Vidal, and Zhang et al. They where all for different types of porous media, core dimensions, boundary conditions and oil/water viscosities. In the analysis conducted by Tavassoli et al., a boundary condition of type OEO was applied to a matrix block of length L. This implies that for the results to be compared to experiments conducted with other boundary conditions, e.g. TEO, TEC and AFO, the length L has to be replaced with the characteristic length L_C, Eq.(2.9) as discussed in the previous section. This then ensures that experimental data in the can be compared to each other. Later in the thesis when we compare the analytical solution to experimental results, the experimental results have already been corrected for using the characteristic length L_C by Tavasolli et al. [19].

3. Oil Recovery during counter-current imbibition

Tavassoli et al. proposed a solution for oil recovery during counter-current imbibition in strongly water wet systems [19]. This chapter focuses on reproducing the model that Tavassoli et al. proposed, but with a more thorough review of the mathematical model and a closer look at how the equations are derived.

First we derive an expression for conservation of water volume in one dimension with no overall flow. We use the extended Buckley-Leverett model as a starting point.

3.1. Derivation of the model

$$\phi \frac{\partial S_l}{\partial t} - \frac{\partial}{\partial x}\left(\frac{K k_{rl}}{\mu_l}\frac{\partial P_l}{\partial x}\right) = 0, \qquad l = o, w \tag{3.1}$$

where S is saturation, K is the permeability k_{rl} is the relative permeability and P_l is the pressure. We define the mobility $\lambda_l = k_{rl}/\mu_l$. The total darcy velocity in the system is

$$U_T = U_w + U_o \tag{3.2}$$

where the phase dependent darcy velocities U_w and U_o are defined as:

$$U_w = -K\lambda_w \frac{\partial P_w}{\partial x} \quad , \quad \lambda_w = k_{rw}/\mu_w \tag{3.3}$$

and:

$$U_o = -K\lambda_o \frac{\partial P_o}{\partial x} \quad , \quad \lambda_o = k_{ro}/\mu_o \tag{3.4}$$

respectively. This gives us the total flux:

$$U = -K\lambda_w \frac{\partial P_w}{\partial x} - K\lambda_o \frac{\partial P_o}{\partial x} \tag{3.5}$$

Using the relation that the capillary pressure P_c is given by:

$$P_c = P_o + P_w \tag{3.6}$$

and inserting into Eq.(3.5) :

$$U = -K\lambda_w \frac{\partial P_w}{\partial x} - K\lambda_o(\frac{\partial P_w}{\partial x} + \frac{\partial P_c}{\partial x}) \tag{3.7}$$

For counter-current flow both the wetting and non-wetting phase flow through one boundary in opposite direction so that the Darcy velocity is zero, that is, there is no net flow [3]. Solving for the resulting pressure term gives:

$$\frac{\partial P_w}{\partial x} = -K\frac{\lambda_o \frac{\partial P_c}{\partial x}}{\lambda_t} \tag{3.8}$$

where $\lambda_t = \lambda_w + \lambda_o$. Substituting Eq.(3.8) into the mass balance equation for the wetting phase gives:

$$\phi\frac{\partial S_w}{\partial t} - \frac{\partial}{\partial x}(K\lambda_w(-\frac{\lambda_o \frac{\partial P_c}{\partial x}}{\lambda_t}) = 0 \tag{3.9}$$

and we rearrange to get:

$$\phi\frac{\partial S_w}{\partial t} + \frac{\partial}{\partial x}(\frac{\lambda_w\lambda_o}{\lambda_t}K\frac{\partial P_c}{\partial x}) = 0 \tag{3.10}$$

Applying the chainrule on the capillary pressure term:

$$\frac{\partial P_c}{\partial x} = \frac{\partial P_c}{\partial S_w}\frac{\partial S_w}{\partial x} \tag{3.11}$$

and substituting this into Eq.(3.10):

$$\phi\frac{\partial S_w}{\partial t} + \frac{\partial}{\partial x}(\frac{\lambda_w\lambda_o}{\lambda_t}K\frac{\partial P_c}{\partial S_w}\frac{\partial S_w}{\partial x}) = 0 \tag{3.12}$$

For simplicity we will refer the non-wetting phase as oil, denoted by subscript o. We can rewrite Eq.(3.12) in terms of dimensionless variables; the normalized water saturation, S, given by Eq.(2.11), and the dimensionless length defined as:

$$x_D = \frac{x}{L} \tag{3.13}$$

using this relation we get:

$$\frac{\partial}{\partial x} = \frac{\partial}{\partial x_D}\frac{\partial x_D}{\partial x} = \frac{\partial}{\partial x_D}\frac{1}{L} \tag{3.14}$$

and rearranging Eq.(2.11) gives:

$$S_w = S(1 - S_{wi} - S_{or}) + S_{wi} \tag{3.15}$$

This yields:

$$\frac{\partial S_w}{\partial t} = (1 - S_{wi} - S_{or})\frac{\partial S}{\partial t} + \frac{\partial S_{wi}}{\partial t} \tag{3.16}$$

S_{wi} is constant with regards to time so the term disappears and we have:

$$\frac{\partial S_w}{\partial t} = (1 - S_{wi} - S_{or})\frac{\partial S}{\partial t} \tag{3.17}$$

same for:

$$\frac{\partial S_w}{\partial x} = \frac{\partial S}{\partial x_D}\frac{\partial S_w}{\partial S}\frac{\partial x_D}{\partial x}\frac{\partial S}{\partial x_D}\frac{(1 - S_{wi} - S_{or})}{L} \tag{3.18}$$

and:

$$\frac{\partial P_c}{\partial S_w} = \frac{\partial P_c}{\partial S}\frac{\partial S}{\partial S_w} = \frac{\partial P_c}{\partial S}\frac{1}{(1 - S_{wi} - S_{or})} \tag{3.19}$$

The boundary conditions for flow in $1 \geq x_D \geq 0$ are as follows:

$$x_D = 0, \quad S = 1 \tag{3.20}$$

$$x_D = 1, \quad \frac{\partial S}{\partial x_D} = 0 \tag{3.21}$$

Inserting equations (3.13), (3.17), (3.18) and (3.19) into Eq.(3.12) and assuming constant permeability K gives us:

$$\frac{\partial S}{\partial t} + \frac{K}{\phi(1 - S_{wi} - S_{or})L^2} \frac{\partial}{\partial x_D}(\frac{\lambda_w \lambda_o}{\lambda_t} \frac{\partial P_c}{\partial S} \frac{\partial S}{\partial x_D}) = 0 \tag{3.22}$$

Instead of attempting to solve the non linear equation 3.22 directly it is proposed by Tavassoli et al. [19] to construct a solution of the weak, or integral form of the equation:

$$\int_0^1 \left[\frac{\partial S}{\partial t} + \frac{K}{\phi(1 - S_{wi} - S_{or})L^2} \frac{\partial}{\partial x_D}(\frac{\lambda_w \lambda_o}{\lambda_t} \frac{\partial P_c}{\partial S} \frac{\partial S}{\partial x_D}) \right] dx_D = 0 \tag{3.23}$$

Let $\bar{S}$ be defined as:

$$\bar{S} = \int_0^1 S dx_D \tag{3.24}$$

Evaluating the integral:

$$\frac{\partial \bar{S}}{\partial t} = \frac{-K}{\phi(1 - S_{wi} - S_{or})L^2} \left[\frac{\lambda_w \lambda_o}{\lambda_t} \frac{\partial P_c}{\partial S} \frac{\partial S}{\partial x_D} \right]_{x_D=0}^{x_D=1} \tag{3.25}$$

Using the boundary condition $\frac{\partial S}{\partial x_D}|_{x_D=1} = 0$ (Eq.(3.21)) we get:

$$\frac{\partial \bar{S}}{\partial t} = \frac{K}{\phi(1 - S_{wi} - S_{or})L^2} \left[\frac{\lambda_w \lambda_o}{\lambda_t} \frac{\partial P_c}{\partial S} \frac{\partial S}{\partial x_D} \right]_{x_D=0} \tag{3.26}$$

Since the oil and water saturations must sum to unity, it becomes apparent that the average normalized water saturation is also a measure of the normalized oil recovery.

Tavassoli et al. notes that the solution to Eq.(3.26) is controlled by a functional form of the capillary pressure and mobilities at the inlet, where S tends to 1 [19].

For convenience Tavassoli et al. [19] assumed the following Corey type functional forms for the mobilities, as described in more detail in sec. 2.3.1, and the imbibition capillary pressure [19][3]. For more flexibility we will assume a LET-functional form of the capillary pressure when we compare the numerical solution of Eq.(3.22) with the analytical solution.

$$\lambda w = \lambda_w^{max} S^a \tag{3.27}$$

$$\lambda o = \lambda_o^{max} (1-S)^b \tag{3.28}$$

$$P_c \;=\; \sigma\sqrt{\frac{\phi}{K}} J(S_w) \tag{3.29}$$

$$\frac{\partial P_c}{\partial S_w} = \sigma\sqrt{\frac{\phi}{K}} \frac{\partial J(S_w)}{\partial S_w} = -\sigma\sqrt{\frac{\phi}{K}} J\,' \tag{3.30}$$

Where $\lambda_o^{max} = K_{ro}^{max}/\mu_o$, $\lambda_w^{max} = K_{rw}^{max}/\mu_w$ and $a, b > 0$.
Using Eq.(3.19) gives:

$$\frac{\partial P_c}{\partial S_w} = \frac{1}{(1-S_{wi}-S_{or})} \frac{\partial P_c}{\partial S} \tag{3.31}$$

combining equations (3.29), (3.30) and (3.31) gives us:

$$\frac{\partial P_c}{\partial S_w}|_{S_w=1-S_{or}} \;=\; -\sigma\sqrt{\frac{\phi}{K}} J\,' = \frac{1}{(1-S_{wi}-S_{or})} \frac{\partial P_c}{\partial S}|_{S=1} \tag{3.32}$$

In Eq.(3.29) Tavassoli et al. [19] assumed Leverett J-function scaling, where $J(S_w)$ is a dimensionless capillary pressure and $-J\,'$ is the dimensionless gradient of the capillary pressure at $S = 1$. We first solve Eq.(3.32) with respect to $\frac{\partial P_c}{\partial S}$ and rewrite Eq.(3.26) with $1 - S = \varepsilon$ and take the limit as $\varepsilon \to 0$ and $x_D \to 0$:

$$\frac{\partial P_c}{\partial S} = -\sigma\sqrt{\frac{\phi}{K}} J'(1-S_{wi}-S_{or}) \tag{3.33}$$

and insert into Eq.(3.26) and we get:

$$\frac{\partial \bar{S}}{\partial t} = \frac{K}{\phi(1 - S_{wi} - S_{or})L^2}\left[\frac{\lambda_w \lambda_o}{\lambda_t} - \sigma\sqrt{\frac{\phi}{K}}J'(1 - S_{wi} - S_{or})\frac{\partial S}{\partial x_D}\right] \tag{3.34}$$

We can rewrite $\frac{\lambda w \lambda o}{\lambda t}$ using the Corey type functional form of the mobilities:

$$\frac{\lambda_w}{\lambda_t}\lambda_o = \frac{\lambda_w^{max} S^a}{\lambda_w^{max} S^a + \lambda_o^{max}(1 - S)^b}\lambda_o^{max}(1 - S)^b \tag{3.35}$$

inserting for $1 - S = \varepsilon$ and knowing that $S \to 1$ as ε approaches zero reduces Eq.(3.35) to:

$$\frac{1}{1}\lambda_o^{max}\varepsilon^b = \lambda_o^{max}\varepsilon^b = \frac{K_{ro}^{Max}\varepsilon^b}{\mu_o} \tag{3.36}$$

inserting this relation into Eq.(3.34) and simplifying it:

$$\frac{\partial \bar{S}}{\partial t} = -\sigma\sqrt{\frac{K}{\phi}}\frac{Kro^{Max}\sigma J'}{\mu_o L^2}\varepsilon^b \frac{\partial S}{\partial x_D}|_{x_D=0} \tag{3.37}$$

We can now define a dimensionless time t_D:

$$t_D = t\sqrt{\frac{K}{\phi}}\frac{\sigma}{\mu_o L^2} \tag{3.38}$$

substituting Eq.(3.38) into Eq.(3.37) is straightforward, and Eq.(3.37) becomes:

$$\frac{\partial \bar{S}}{\partial t_D} = Kro^{Max} J'\varepsilon^b \frac{\partial S}{\partial x_D}|_{x_D=0} \tag{3.39}$$

As Tavassoli et al. noted and we also observed, the oil mobility λ_o disappears for $\varepsilon = 0$, it is therefore required that either $\frac{\partial S}{\partial x_D}$ or $\frac{\partial P_c}{\partial S}$ diverges at $x_D = 0$ to obtain reasonable solutions to Eq.(3.39) [19]. Tavassoli et al. further state that if an assumption of a finite capillary pressure gradient is made, this means that the saturation gradient must be infinite at $x_D = 0$. This is in agreement with earlier numerical solutions of the problem [19]. From the inlet boundary condtition, Eq.(3.21), Tavassoli et al. [19] notes that the oil saturation is at residual value when the mobility is zero. However, to allow oil to flow out of the system despite this, an infinte saturation gradient is needed to ensure a finite oil flow rate [19].

The time scale for imbition given by t_D, Eq.(3.38), is similar to Eq.(2.8), except for the scaling with viscosity as noted in sec. 2.5.1 . The solution presented by Tavassoli is inversely proportional to the oil viscosity and is independent of the water viscosity.

3.2. Early time solution

Tavassoli et al. first proposed an early time solution, that is, before the saturation front reaches the boundary. This solution is also equivalent to imbibition in a semi-infinite medium. Tavassoli et al. [19] proposed a simple analytical form for the spatial variation of the saturation. That makes us able to find the time-dependent coefficients that obey equation (3.37) and the boundary conditions.

The boundary conditions specified by Tavassoli et al. [19] are as follows:

$$S(x_D, t_D) = 1 - A(t_D)x_D^f; \qquad x_D \leq x_D^0, \quad 0 < f < 1 \tag{3.40}$$

$$S(x_D, t_D) = 0 \qquad x_D \geq x_D^0 \tag{3.41}$$

This obeys the boundary condition at $x_D = 0$, $x_D^0(t_D)$ is the length where the saturation first becomes zero. Since $S(x_D^0, t_D) = 0$, we can find an expression for x_D^0 from Eq.(3.40):

$$0 = 1 - A(t_D)x_D^f$$

$$1 = A(t_D)x_D^f$$

$$x_D^0 = (\frac{1}{A(t_D)})^{\frac{1}{f}} = A(t_D)^{-1/f} \tag{3.42}$$

and the average saturation can be found by integrating $S(x_D, t_D)$ from 0 to x_D^0:

$$\bar{S}(t_D) = \int_0^{x_D^0} S dx_D = \int_0^{x_D^0} 1 - A(t_D)x_D^f dx_D$$

$$\bar{S}(t_D) = x_D - A(t_D)\frac{1}{f+1}x_D^{f+1}|_{x_D=0}^{x_D=x_D^0}$$

$$\bar{S}(t_D) = x_D^0 - A(t_D)\frac{1}{f+1}x_D^{0\,f+1} \tag{3.43}$$

inserting Eq.(3.42) in Eq.(3.43) gives us:

$$\bar{S}(t_D) = A(t_D)^{-1/f} - A(t_D)\frac{1}{f+1}(A(t_D)^{-1/f})^{\,f+1}$$

$$\bar{S}(t_D) = A(t_D)^{-1/f} - \frac{1}{f+1}A(t_D)\,(A(t_D)^{-1})\,(A(t_D)^{-1/f}\,)$$

$$\bar{S}(t_D) = A(t_D)^{-1/f}(1 - \frac{1}{f+1}) = A(t_D)^{-1/f}\frac{f}{f+1} = \frac{f}{(f+1)A(t_D)^{1/f}} \tag{3.44}$$

We will use Eq.(3.39) to find an expression for $A(t_D)$. First we find ε as a function of $A(t_D)$ using the boundary conditions in Eq.(3.40):

$$1 - S = A(t_D)x_D^f$$

and since $\varepsilon = 1 - S$:

$$\varepsilon = A(t_D)x_D^f$$

We evaluate the left hand side of Eq.(3.39) :

$$\frac{\partial \bar{S}}{\partial t_D} = \frac{\partial}{\partial t_D}A(t_D)^{-1/f}\frac{f}{f+1} = -\frac{1}{f}A(t_D)^{-1/f-1}\frac{f}{f+1}\frac{\partial A(t_D)}{\partial t_D} = -\frac{A(t_D)^{-1/f-1}}{1+f}\frac{\partial A(t_D)}{\partial t_D}$$

and then the right hand side:

$$Kro^{Max}J'\varepsilon^b\frac{\partial S}{\partial x_D}|_{x_D=0}$$

$\frac{\partial S}{\partial x_D}|_{x_D=0}$ where $S = 1 - A(t_D)x_D^f$ gives:

$$\frac{\partial S}{\partial x_D} = A(t_D)fx_D^{f-1} = A(t_D)f\frac{1}{x_D^{1-f}} \tag{3.45}$$

and from the relation that $\varepsilon = A(t_D)x_D^f$ we get that $\frac{1}{x_D^{1-f}} = \frac{A^{\frac{1-f}{f}}}{\varepsilon^{\frac{1-f}{f}}}$. Inserting this in Eq.(3.45) we see that:

$$\frac{\partial S}{\partial x_D} = A(t_D) f \frac{A(t_D)^{\frac{1-f}{f}}}{\varepsilon^{\frac{1-f}{f}}} = \frac{f A(t_D)^{\frac{1}{f}}}{\varepsilon^{\frac{1-f}{f}}} \tag{3.46}$$

Now the right hand side becomes:

$$Kro^{Max} J' \varepsilon^b \frac{f A(t_D)^{\frac{1}{f}}}{\varepsilon^{\frac{1-f}{f}}} = Kro^{Max} J' f \varepsilon^{b+1-1/f} A(t_D)^{\frac{1}{f}} \tag{3.47}$$

and combining left and right hand side gives for Eq.(3.39):

$$-\frac{A(t_D)^{-1/f-1}}{1+f} \frac{\partial A(t_D)}{\partial t_D} = -Kro^{Max} J' f \varepsilon^{b+1-1/f} A(t_D)^{\frac{1}{f}} \tag{3.48}$$

for the right hand side of Eq.(3.48) to be finite when ε–> 0 we require $f = \frac{1}{1+b}$
This specifies f and gives acceptable solutions for any $b > 0$, let ε–> 0 and Eq.(3.48) becomes:

$$\frac{A(t_D)^{-1-2/f}}{f(1+f)} \frac{\partial A(t_D)}{\partial t_D} = -Kro^{Max} J' \tag{3.49}$$

To find an expression for $A(t_D)$ we integrate Eq.(3.49) once:

$$\int A(t_D)^{-1-2/f} \, \partial A(t_D) = \int -Kro^{Max} J' f(1+f) \, \partial t_D \tag{3.50}$$

integrating left hand side with regards to $A(t_D)$ and right hand side with regards to ∂t_D and we get:

$$-\frac{1}{2} f A(t_D)^{-2/f} = -Kro^{Max} J' f(1+f) \, t_D + C \tag{3.51}$$

where C is a constant. Rearranging Eq.(3.51) yields:

$$A(t_D)^{-2/f} = \frac{2Kro^{Max} J' f(1+f)}{f} \, t_D + C \tag{3.52}$$

inserting for $f = \frac{1}{1+b}$ on the right hand side and we get:

$$\frac{2Kro^{Max}J'f(1+f)}{f}\,t_D + C = \frac{2(2+b)}{1+b}\,Kro^{Max}J't_D + C \tag{3.53}$$

set:

$$\beta = \frac{2(2+b)}{1+b}\,Kro^{Max}J' \tag{3.54}$$

and we have:

$$A(t_D)^{-2/f} = \beta\,t_D + C \tag{3.55}$$

$$A(t_D) = (\beta\,t_D + C)^{-f/2} \tag{3.56}$$

$$A(t_D) = \frac{1}{(\beta\,t_D + C)^{f/2}} \tag{3.57}$$

Inserting Eq.(3.57) into Eq.(3.44) and choosing the constant $C = 0$ to obey the initial condition that $x_D^0(0) = \overline{S}(0) = 0$. gives us:

$$\overline{S} = \frac{f}{(f+1)(\frac{1}{(\beta\,t_D)^{f/2}})^{1/f}} \tag{3.58}$$

$$\overline{S} = \frac{f}{(f+1)}(\beta\,t_D)^{1/2} \tag{3.59}$$

$$\overline{S} = \frac{1}{(2+b)}(\beta\,t_D)^{1/2} \tag{3.60}$$

$$\overline{S} = (\frac{\beta}{(2+b)^2}\,t_D)^{1/2} \tag{3.61}$$

$$\overline{S} = (\gamma\, t_D)^{1/2} \tag{3.62}$$

where:

$$\gamma = \frac{\beta}{(2+b)^2} = \frac{2}{(1+b)(2+b)}\, Kro^{Max} J' \tag{3.63}$$

combining equations 3.42 and 3.57 we get an expression that shows how the leading edge of the water front advances:

$$x_D^0(t_D) = (\beta\, t_D)^{1/2}$$

This solution is valid for $t_D \leq t_{D1}$ until the water reaches the boundary, when $x_D^0(t_D = t_{D1}) = 1$, and we have:

$$1^2 = \beta\, t_{D1} \tag{3.64}$$

$$t_{D1} = \frac{1}{\beta} \tag{3.65}$$

3.3. Late time solution

For late times, $t_D \geq t_{D1}$, Tavassoli et al. proposed a similar functional form for the saturation profile:

$$S(x_D, t_D) = 1 - A(t_D)x_D^f + B(t_D)x_D; \qquad 0 \leq x_D \leq 1, \quad 0 < f < 1 \tag{3.66}$$

The extra linear term B in x_D is added to fulfill the no flux constraint at $x_D = 1$, $\frac{\partial S}{\partial x_D}|_{x_D=1} = 0$. So:

$$B(t_D) = fA(t_D) \tag{3.67}$$

and Eq.(3.66) becomes:

$$S(x_D, t_D) = 1 - A(t_D)\,(x_D^f - f x_D) \tag{3.68}$$

The average saturation is:

$$\bar{S}(t_D) = \int_0^1 S dx_D = \int_0^1 1 - A(t_D)\,(x_D^f - f x_D)\,dx_D \tag{3.69}$$

$$\bar{S}(t_D) = x_D - A(t_D)\,(\frac{x_D^{f+1}}{f+1} - \frac{f x_D^2}{2})|_{x_D=0}^{x_D=1} \tag{3.70}$$

$$\bar{S}(t_D) = 1 - A(t_D)\,(\frac{1}{f+1} - \frac{f}{2}) \tag{3.71}$$

We can now use Eq.(3.39) to find $A(t_D)$ in the limit as $\varepsilon \to 0$, $x_D \to 0$ as we did for the early time solution and insert Eq.(3.45) for ε:

$$(\frac{1}{f+1} - \frac{f}{2})\frac{\partial A(t_D)}{\partial t_D} = -Kro^{Max} J' f \varepsilon^{b+1-1/f} A(t_D)^{\frac{1}{f}} \tag{3.72}$$

For Eq.(3.72) to be finite in the limit when $\varepsilon \to 0$, it is once again required that $f = \frac{1}{1+b}$, inserting this in Eq.(3.72) gives us:

$$\frac{1}{A(t_D)^{1+b}}\frac{\partial A(t_D)}{\partial t_D} = -Kro^{Max} J' f A(t_D)^{\frac{1}{f}} \frac{1}{(\frac{1}{f+1} - \frac{f}{2})} \tag{3.73}$$

which becomes:

$$\frac{1}{A(t_D)^{1+b}}\frac{\partial A(t_D)}{\partial t_D} = -\frac{2(2+b)}{b(3+2b)} Kro^{Max} J' \tag{3.74}$$

integrating Eq.(3.74) to find a new expression for $A(t_D)$:

$$A(t_D) = \frac{1}{(\eta t_D + C)^{1/b}} \tag{3.75}$$

where:

$$\eta = \frac{1+b}{3+2b}\beta = \frac{2(2+b)}{(3+2b)}Kro^{Max}J' \tag{3.76}$$

and C is a constant, Tavassoli et al. determined the constant by insisting that the average saturation is continous at $t_D = t_{D1}$. From early time solution Eq.(3.62), and late time solution Eq.(3.71) and Eq.(3.75) the constant C becomes:

$$C = \left[\frac{b(3+2b)}{2(1+b)^2}\right]^b - \eta t_{D1} \tag{3.77}$$

Then we can write:

$$\bar{S}(t_D) = 1 - \frac{1+b}{(2+b)(1+\kappa(t_D - t_D))^{1/b}} \tag{3.78}$$

where:

$$\kappa = \left[\frac{2(2+b)}{3+2b}\right]\left[\frac{2(1+b)^2}{b(3+2b)}\right]^b Kro^{Max}J' \tag{3.79}$$

4. Solution of the model

In this section we will look at the analytical solution to the diffusion equation as it has been derived in sec. 3.1, and reproduce the solution presented by Tavassoli et al. [19] using MATLAB. We will also attempt to produce a numerical solution to the problem by creating a discrete scheme. The discrete scheme will serve as a basis for comparing the analytical and numerical solutions.

4.1. Analytical solution

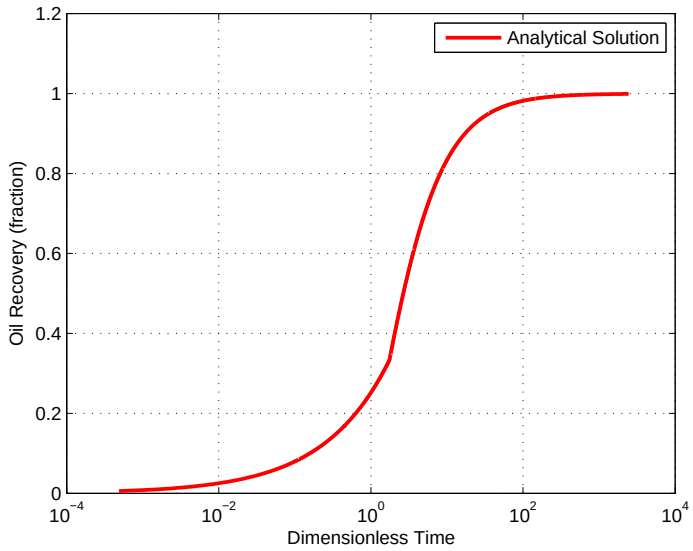

Figure 4.1.: Analytical solution of the model proposed by Tavassoli et al. [19], that we reproduced in sec. 3.1.

Fig. 4.1 shows the solution of the model derived in sec. 3.1. The solution is plotted as a continuous curve consisting of the early time solution, Eq.(3.62) and the late time solution, Eq.(3.78) as a function of dimensionless time t_D, Eq.(3.38).

The analytical solution derived in the previous chapter has been proven to match experimental data quite well [19] as we can see in Fig. 4.2, where the solution is plotted together with experimental data from three different authors. As mentioned in sec. 2.5.2 the experiments conducted by Mattax and Kyte, Hamon and Vidal, and

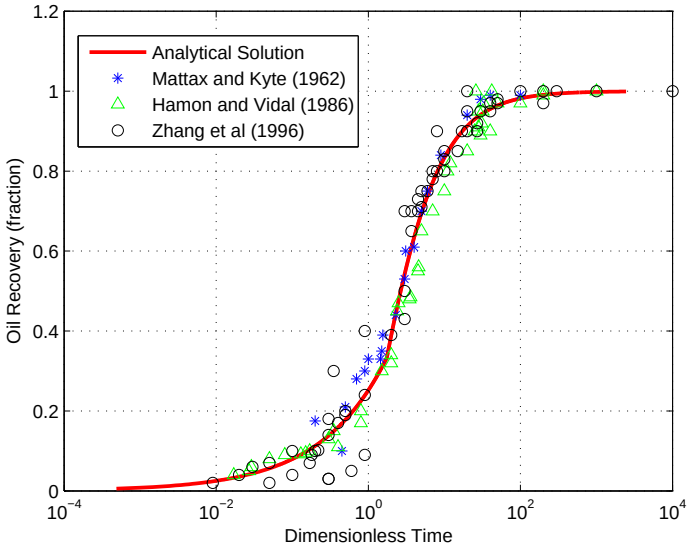

Figure 4.2.: Figure showing the analytical solution derived in chapter sec. 3.1 compared with experimental oil recovery data as a function of dimensionless time

Zhang et al. have been conducted with different boundary conditions for the core samples. Tavassoli et al. [19] obtained the experimental oil recoveries as a function of time and plotted them as a function of dimensionless time t_D, Eq.(3.38). We would like to note that since we did not aquire the experimental data ourselves, the experimental data presented in this thesis is plotted from figures in Tavassoli et al.

4.1.1. Early and late time solutions

Fig. 4.3 shows analytical recovery for both the early and late time solutions. It is worth noting that the early time solution increases with the square root of time as we can see from Eq.(3.62). Tavassoli et al. explaines that the reason for this behaviour is that the advance rate is proportional to the capillary pressure gradient, which is inversely proportional to the distance the waterfront has already travelled [19]. We observe that the solutions intersect in the point where the water reaches the boundary, $t_{D1} = 1.7544$. From Fig. 4.1, where the solution is plotted as a continous function, it is also possible to observe a small change in the gradient of the curve in that same point. One explanation for this change in gradient may result from the fact that Tavassoli et al. [19] only made a requirement that there is continuity in $\bar{S}(t)$, and not in $\bar{S}'(t)$. From Fig. 4.4 we see that the experimental data gives a good match with the early time solution until it reaches t_{D1} and for $t_D > t_{D1}$ the experimental data matches the late time solution.

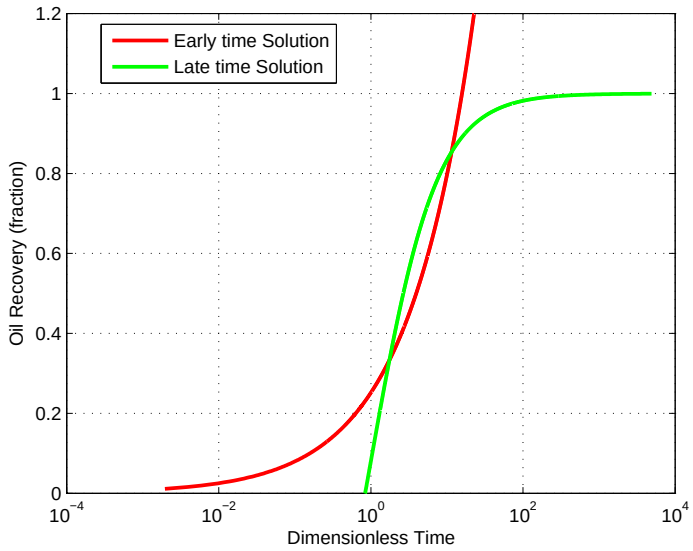

Figure 4.3.: Figure showing analytical recovery solution versus dimensionless time for early and late time solutions.

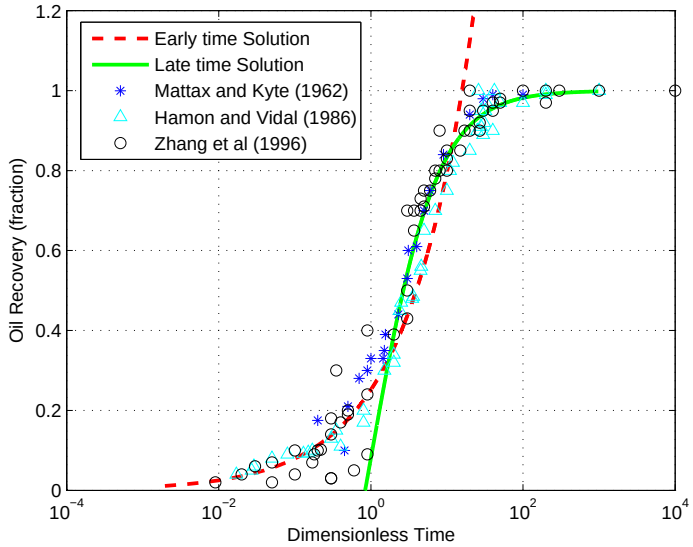

Figure 4.4.: Figure showing early- and late time solutions vs. experimental data

4.1.2. Dependence on parameters

The expressions derived for the average water saturation, which corresponds to the normalized oil recovery, are dependent on three multiphase flow properties; The Corey oil maximum relative permeability, K_{ro}^{max}, the Corey oil relative permeability exponent, b, and the dimensionless capillary pressure gradient, that is, $J´$ at $S = 1$. For the early time solution this dependence is expressed through the relation γ, Eq.(3.63), and for the late time solution through κ, Eq.(3.79). It is important to note that changing parameters in the model only affect the rate at which recovery is achieved, not the recovery efficiency. The overall recovery efficiency is dependent on residual oil saturation, which we have assumed constant at a value of 0.25 throughout this thesis.

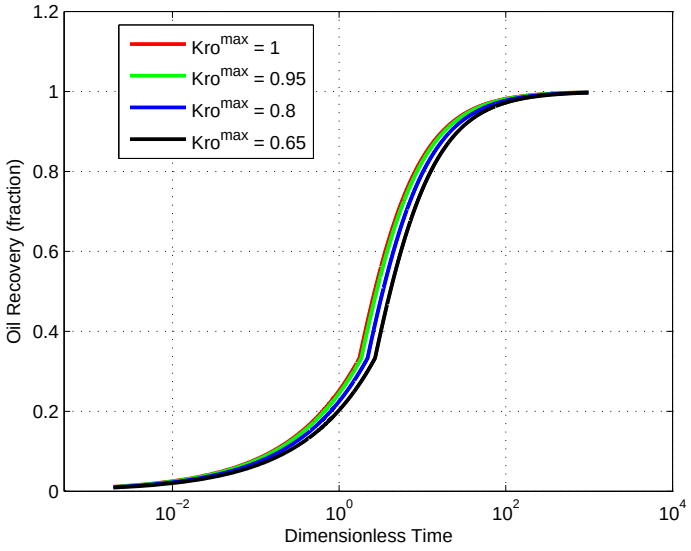

Figure 4.5.: Figure showing oil recovery vs. dimensionless time for different values of the maximum oil relative permeability, K_{ro}^{max}.

Fig. 4.5 shows the recovery plotted vs. dimensionless time for different K_{ro}^{max} values ranging from 1 to 0.65. It is apparent that the imbibition process is more effective for higher values of K_{ro}^{max}. This is readily explained through the relationship with κ, Eq.(3.79) for late time solutions and the variable β Eq.(3.54) found in the early time solution variable γ, Eq.(3.63). In both solutions we note that the solution varies proportionally with the value of K_{ro}^{max}.

Tavassoli et al. state in [19] that the value for dimensionless capillary pressure gradient at S=1, which in the paper is 0.19, corresponds to typical imbibition pressures given by Bear [3], which give similiar or larger values for $J´$on sand and bead-packs. When testing the sensitivity to different $J´$ values we will therefore use values between 0.15 and 0.30. We see from figure Fig. 4.6 that the solution gives a more effective imbibition process for higher dimensionless capillary pressure gradients.

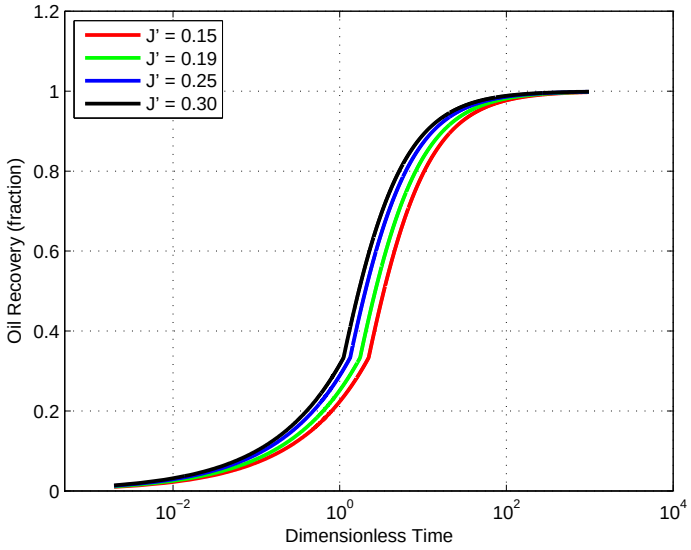

Figure 4.6.: Figure showing oil recovery vs. dimensionless time for different values of the dimensionless capillary pressure gradient, $J´$.

This is through the same relations that we mentioned in context with K_{ro}^{max} above, both early and late time solutions vary proportionally with the value of $J´$. Later in the thesis we will investigate further to see how letting $\bar{S}(t)$ only be dependent on $J´$ in the point $S = 1$, and ignoring $J´$ for $S \in [0, 1]$, will affect the solution.

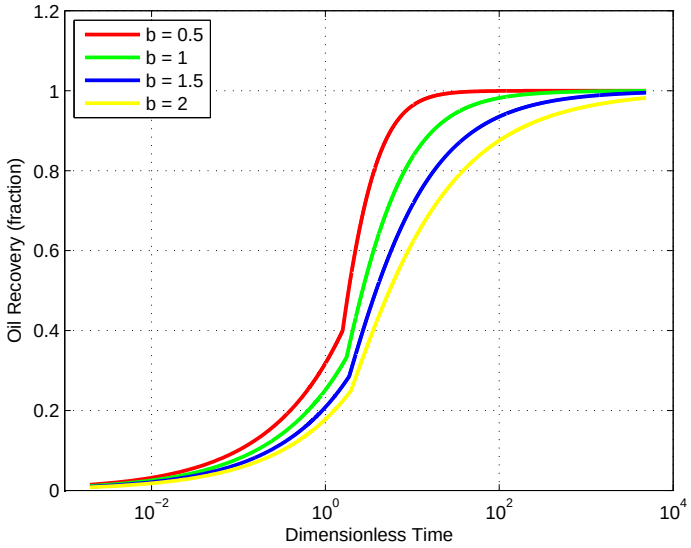

Figure 4.7.: Figure showing Oil Recovery vs. dimensionless time for different values of the Corey oil exponent, b.

The Corey oil relative permeability exponent b is set to 1 in [19] and has to fulfill

$b > 0$, referring to conditions for Eq.(3.27) and (3.28). When varying b-values we see from Fig. 4.7 that the recovery process is more effective for lower values. The Corey oil exponent also alters the shape of the recovery curve, especially for late time solutions, and much more so than varying the K_{ro}^{max} and $J´$ values. This can also be explained through the relationship with κ, Eq.(3.79) for late time solutions, and the variable β Eq.(3.54) found in the early time solution variable γ, Eq.(3.63). However, we note that the dependence on b in the solutions is more complex than for K_{ro}^{max} and $J´$. Especially for the late time solution κ, Eq.(3.79) since b is also an exponent in this nonlinear expression. This accounts for the considerable changes in the shape of the curve for late times and varying b-values observed in Fig. 4.7. The premise for using $b = 1$ in the paper is that for steady state waterflooding data for strongly water-wet Berea sandstone, the oil relative permeability varies approximately linearly with saturation.

It becomes apparent when looking at the figures Fig. 4.5, Fig. 4.6 and Fig. 4.7 that the Corey oil relative permeability exponent b is the parameter that has the greatest effect on the model. Another important thing to note is how the transition from early to late time solutions change for varying values of K_{ro}^{max}, $J´$ and b. The time when the change occurs is termed t_{D1}, Eq.(3.65) and is given by $\frac{1}{\beta}$. Since β varies proportionally with K_{ro}^{max} and $J´$ we can see from Fig. 4.5 and Fig. 4.6 that lower values of the parameters give a transition from early to late time solutions at a later time, t_D. For example, $K_{ro}^{max} = 1$, $b = 1$ and $J´ = 0.19$ gives $t_{D1} = 1.7544$. However, if we change K_{ro}^{max} to 0.65, we get $t_{D1} = 2.6991$. This implies that the imbibition front meets the boundary at a later time, which means that the rate of recovery is slower. For b the change in transition time is more complex, but we note that for lower values of b we have an earlier transition, and also a higher recovery in the point of transition, referring to Fig. 4.7.

4.1.3. Recovery vs. Distance

In this section we would like to see how the model behaves if we plot $S(x_D, t_D)$ instead of $\bar{S}(t_D)$. It is important to note that the area under the saturation profile is equal to the recovery. Note that $t_D = t_{D1}$ is the time for transition between the early and late time solution.

The solution proposed by Tavassoli et al. [19] gives a good correlation between early and late time (before and after meeting the boundary) data when we plot $\bar{S}(t)$. However, if we plot $S(x_D, t_D)$ for a fixed time instead, we can see that there is a discontinuity between the solutions when $t_D = t_{D1} = 1.7544$. Referring to Fig. 4.8 we see that for the exact same time, the saturation profile is quite different for early and late time solutions. The area under the graph is equal for both early and late time solutions so the condition that the average saturation, $\bar{S}(t_D)$, is continuous at $t_D = t_{D1}$ is still valid, but we see that this is not the case when plotted as a function of the spatial variable x_D. This is most likely due to the fact that Tavassoli et al. [19] only made the requirement that there is continuity in $\bar{S}(t)$ and not in $S(x_D, t_D)$.

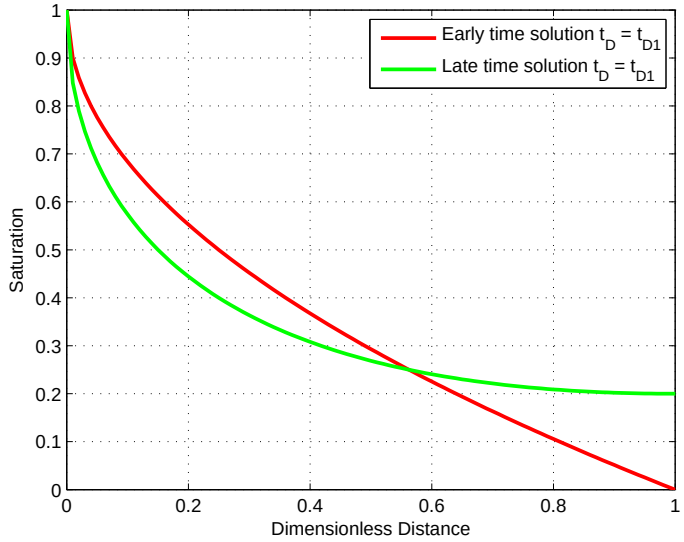

Figure 4.8.: Figure showing $S(x_D, t_D)$ for both early and late times at exactly the same time $t_D = t_{D1} = \frac{1}{\beta} = 1.7544$

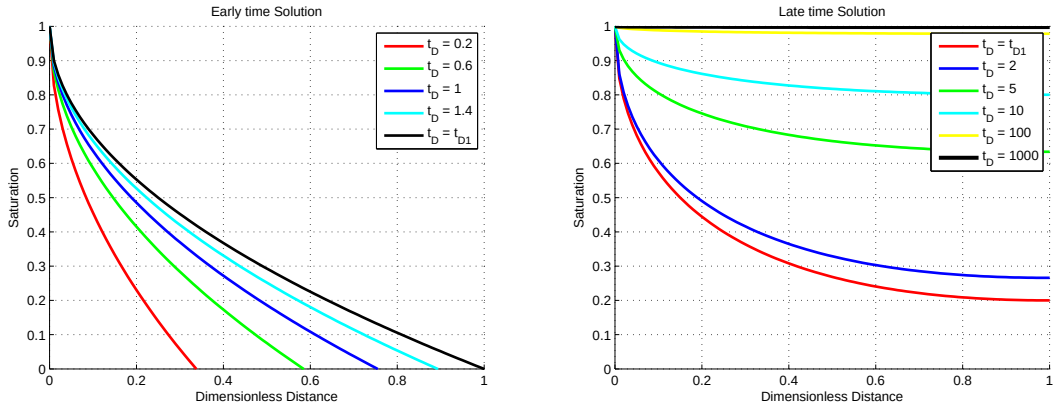

(a) $S(x_D, t_D)$ for early time solution.

(b) $S(x_D, t_D)$ for late time solution.

Figure 4.9.: Figure showing $S(x_D, t_D)$ for given t_D for both early and late time solutions.

From 4.9a we note that for $t_D = t_{D1}$, the saturation profile is at $x_D = 1$ as we expected since $x_D = 1$ is the location of the boundary, this is however not the case for the late time solution in $t_D = t_{D1}$ where we see that the water has already passed the boundary. Looking at 4.9b we see that for $t_D = 1000$ the sample/reservoir is fully saturated, that is $S = 1$ for all x_D. Since the area under the profile is equal to recovery, this means that the recovery is 100% in this case, which is confirmed by Fig. 4.1.

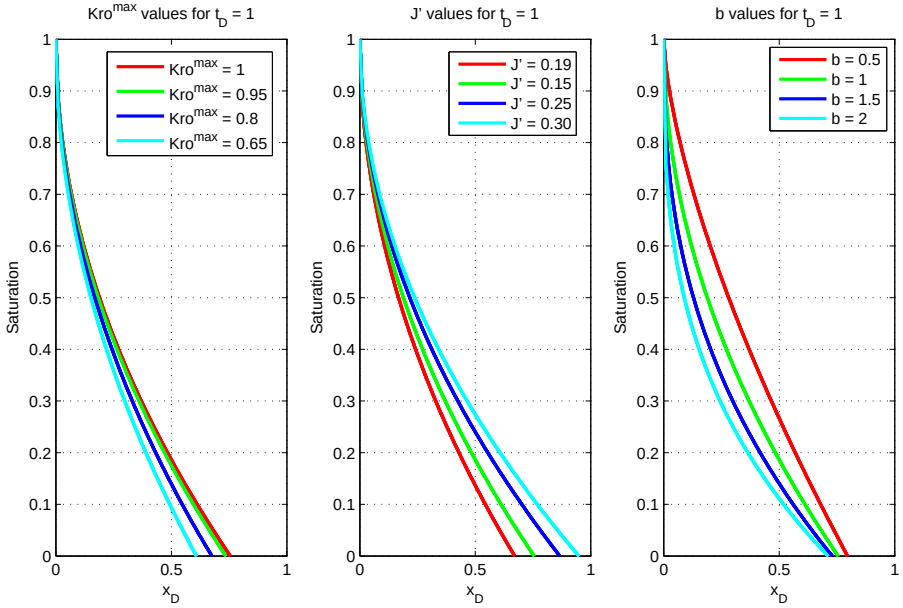

Figure 4.10.: Figure showing the model's depence on the three multiphase flow properties when plotting saturation vs. dimensionless distance, $S(x, t_D = 1)$.

Fig. 4.10 shows how the model depend on the three multiphase flow properties when plotting $S(x_D, t_D = 1)$. As mentioned before, the recovery of oil is simply the area under the graph so our results when varying the properties when plotting $S(x_D, t_D)$ corresponds to our findings when plotting $\bar{S}(t_D)$. We see that the saturation front has travelled longer for higher K_{ro}^{Max} and J' values which corresponds to the higher recovery seen from the same values in figure Fig. 4.5 and Fig. 4.6. The b curve is as mentioned slightly different because the b parameter changes the shape of the curve due to a more complex relation in the solution. We see that, starting from the lowest value of b, the saturation profile goes from almost linear to more convex as we increase the b-value.

4.2. Numerical solution

The differential Eq.(3.22) cannot, in general, be solved analytically. We need to discretize it for all variables so that we can solve it numerically by the use of a numerical scheme. This leads us to a set of algebraic equations. We subdivide the reservoar into smaller parts, grid blocks, and we divide the time axis into finite time intervals. We see that the equation is a second order derivative with regards to x and we will end up with an equation on the form $u_t = (a(u)u_x)_x$

4.2.1. Deriving the numerical scheme

We have the equation:

$$\frac{\partial S}{\partial t} + \frac{K}{\phi(1 - S_{wi} - S_{or})L^2}\frac{\partial}{\partial x_D}(\frac{\lambda w \lambda o}{\lambda t}\frac{\partial P_c}{\partial S}\frac{\partial S}{\partial x_D}) = 0 \tag{4.1}$$

We can rewrite $\frac{\lambda w \lambda o}{\lambda t}(S)$ as a function of fractional flow and the mobility of oil. Fractional flow is given by:

$$f = \frac{\frac{k_{rw}}{\mu_w}}{\frac{k_{rw}}{\mu_w} + \frac{k_{ro}}{\mu_o}} = \frac{1}{1 + \frac{\mu_w}{\mu_o}\frac{k_{ro}}{k_{rw}}} = \frac{\lambda_w}{\lambda_t} \tag{4.2}$$

we see that $\frac{\lambda w \lambda o}{\lambda t}(S)$ can be written as:

$$\frac{\lambda_w \lambda_o}{\lambda_t}(S) = f(S)\,\lambda_o(S) \tag{4.3}$$

substituting the capillary pressure P_c with the dimensionless capillary pressure J:

$$P_c(S) = \sigma\sqrt{\frac{\phi}{K}}J(S) \tag{4.4}$$

Inserting equations (4.3) and (4.4) into Eq.(4.1) and we have:

$$\frac{\partial S}{\partial t} + \frac{K}{\phi(1 - S_{wi} - S_{or})L^2}\frac{\partial}{\partial x_D}\left(f(S)\,\lambda_o(S)\,\sigma\sqrt{\frac{\phi}{K}}\frac{\partial J}{\partial S}\frac{\partial S}{\partial x_D}\right) = 0 \tag{4.5}$$

Introducing dimensionless time given by Eq.(3.38):

$$t_D = t\sqrt{\frac{K}{\phi}}\frac{\sigma}{\mu_o L^2} \tag{4.6}$$

and Eq.(4.5) reduces to:

$$\frac{\partial S}{\partial t_D} + \frac{K_{ro}^{Max}}{(1 - S_{wi} - S_{or})}\frac{\partial}{\partial x_D}\left(f(S)\, k_{ro}(S)\, \frac{\partial J}{\partial S}\frac{\partial S}{\partial x_D}\right) = 0 \tag{4.7}$$

which in a simpler form we can write:

$$\frac{\partial S}{\partial t} + \omega\frac{\partial}{\partial x_D}\left(a(S)\frac{\partial J}{\partial x_D}\right) = 0 \tag{4.8}$$

where:

$$\omega = \frac{k_{ro}^{Max}}{1 - S_{wi} - S_{or}} \tag{4.9}$$

and:

$$a(S) = f(S)\, k_{ro}(S) \tag{4.10}$$

where $a(S)$ is the non-linear diffusion coefficient.

We use shorthand notation (and drop the subscript D in t and x) and write Eq.(4.8) as:

$$\partial_t S + \omega\partial_x(a(S)\partial_x J(S)) = 0 \tag{4.11}$$

Corresponding to Tavassoli et al.'s results [19] we set $k_{ro}^{Max} = 1$. As mentioned before we have set $S_{or} = 0.25$, and we will also set $S_{wi} = 0.25$. These values of k_{ro}^{Max}, S_{wi} and S_{or} will remain constant for the rest of the thesis unless otherwise stated. Since Tavassoli et al. has used a dimensionless capillary gradient $-J'(S_w) = 0.19$ it is important for comparison that we choose parameters for our capillary pressure that give $-\frac{1}{(1-S_{wi}-S_{or})}J'(S) \approx 0.19$ at $S = 1$ (that is, $S_w = 1 - S_{or}$)

Using an explicit numerical scheme and evaluating at the grid boundaries we get:

$$\partial_t S \approx \frac{1}{\triangle t}(S_j^{n+1} - S_j^n) \tag{4.12}$$

$$\partial_x(a(S)\partial_x J(S)) \approx \frac{1}{\triangle x}\left(a(S)^n_{j+\frac{1}{2}}\partial_x J(S)^n_{j+\frac{1}{2}} - a(S)^n_{j-\frac{1}{2}}\partial_x J(S)^n_{j-\frac{1}{2}}\right) \tag{4.13}$$

The terms for $a(S)$ and J can be approximated by:

$$a(S)^n_{j+\frac{1}{2}} = f(S)^n_j\, k_{ro}(S)^n_{j+1}, \qquad a(S)^n_{j-\frac{1}{2}} = f(S)^n_{j-1}\, k_{ro}(S)^n_j \tag{4.14}$$

and:

$$J(S)^n_{j+\frac{1}{2}} = \frac{J(S)^n_{j+1} - J(S)^n_j}{\triangle x}, \qquad J(S)^n_{j-\frac{1}{2}} = \frac{J(S)^n_j - J(S)^n_{j-1}}{\triangle x} \tag{4.15}$$

with this we can rewrite eq 4.11 and solve for the next timestep S_j^{n+1}:

$$S_j^{n+1} = S_j^n - \omega\frac{\triangle t}{\triangle x^2}\left(f(S)^n_j\, k_{ro}(S)^n_{j+1}\left[J(S)^n_{j+1} - J(S)^n_j\right] - f(S)^n_{j-1}\, k_{ro}(S)^n_j\left[J(S)^n_j - J(S)^n_{j-1}\right]\right) \tag{4.16}$$

Eq.(4.16) represents the numerical scheme that we will use to solve the model.

4.2.1.1. Discretization at the boundary:

Above we have discretized the equation in the interior part of the domain, we also have to evaluate the boundaries, that is, block $j = 1$ and block $j = K$

From sec. 3.1 we remember that we have the following boundary conditions to consider for $1 \geq x_D \geq 0$:

$$x_D = 0, \quad S = 1 \tag{4.17}$$

$$x_D = 1, \quad \frac{\partial S}{\partial x_D} = 0 \tag{4.18}$$

which gives us for $j = 1$:

$$S_1^{n+1} = S_1^n - \omega \frac{\triangle t}{\triangle x} \left(f(S)_1^n \, k_{ro}(S)_2^n \frac{J(S)_2^n - J(S)_1^n}{\triangle x} - f(S)_0^n \, k_{ro}(S)_1^n \frac{J(S)_1^n - J(S)_0^n}{\triangle x/2} \right) \tag{4.19}$$

and for cell $j = K$:

$$S_K^{n+1} = S_K^n - \omega \frac{\triangle t}{\triangle x} \left(0 - f(S)_{K-1}^n \, k_{ro}(S)_K^n \frac{J(S)_K^n - J(S)_{K-1}^n}{\triangle x} \right) \tag{4.20}$$

It is obvious that the driving force in the simulator is the difference in capillary pressure between the outside face and the first grid block. Since the boundary condition for the left end face states that it is fully contacted by water ($S = 1$) and first grid block is at zero intial saturation (from the intitial conditions), we see that the driving force is maximum in the beginning of the simulation and diminishes as the difference in saturations becomes less between the grid blocks.

4.2.2. Stability criteria

Applying a difference scheme and discretising an equation gives rise to a computational error, which can affect the numerical stability of the solution.

"A difference scheme is called stable if a computational error introduced at one time step does not grow at computations for subsequent time steps."[10]

To ensure numerical stability we introduce a stability criteria. We can say that our difference scheme is stable if it fulfills this criteria:

$$\omega \frac{\triangle t}{\triangle x^2} \, | \, f(S) \, k_{ro}(S) | \leq 0.5 \tag{4.21}$$

In this thesis we have ensured that we have used a $\triangle t$ sufficiently large to satisfy the criteria mentioned above.

5. Comparing the models

While the analytical model, due to the approximations that have been used, is only dependent on three multiphase properties, the numerical model has much more flexibility in that we can change any parameter we like. This makes it very useful for revealing the analytical models shortcomings and can give us a good indication of how well it behaves, and will also allow us to assess the validity of the assumptions that have been made. In this chapter we will therefore study the effects of changing different parameters related to relative permeability, capillary pressure and viscosity. While the analytical solution can be considered exact and stable, the numerical model is dependent on grid size and timestep refinement so we will also include a study that illustrates the effect of changing grid size. Unless otherwise stated all numerical solutions have been run with grid size, $\Delta x = \frac{1}{50}$. As mentioned in sec. 4.1.2 it is important to note that changing the model's parameters only affect the rate at which a recovery is achieved, not the recovery efficiency. The overall recovery efficiency is dependent on residual oil saturation which, as mentioned, is assumed constant at a value of 0.25.

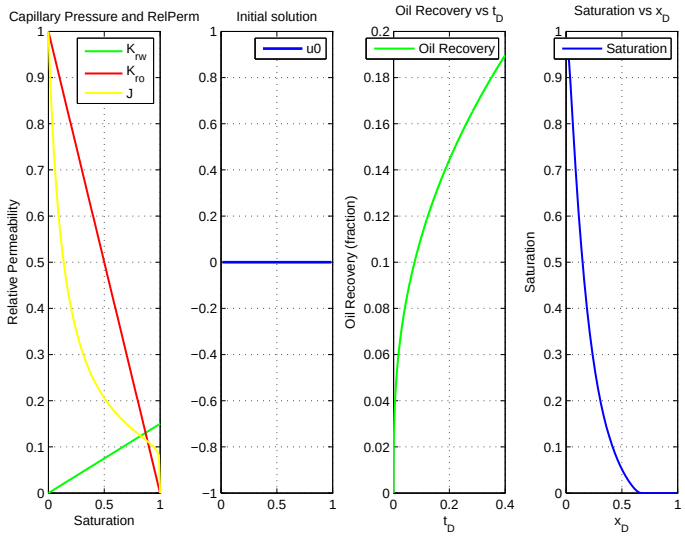

Figure 5.1.: Figure showing an example of the numerical solution where we have plotted the relative permeability and capillary pressure functions, the initial solution, the oil recovery vs. time, and the saturation profile for $t_D = 0.4$.

Now, we have ensured that the parameters that the analytical model depends on

are the same in the numerical model, so $b = 1$, $K_{ro}^{Max} = 1$ and $J' = 0.19$ at $S = 1$. The analytical model, however, says nothing about, for instance, the values of the Corey relative permeability parameters a and K_{rw}^{Max} from sec. 2.3.1, or how J' behaves for $S \in [0, 1]$. The numerical model also depend on oil and water viscosity through the fractional flow term in $a(S)$, Eq.(4.2) and (4.10). We will introduce a viscosity ratio μ_r in sec. 5.3 and the effect it has on the solution will be discussed. As mentioned before we have created a capillary pressure function that gives a dimensionless capillary pressure gradient, $J' = 0.19$ using the LET-correlation from sec. 2.4.2.

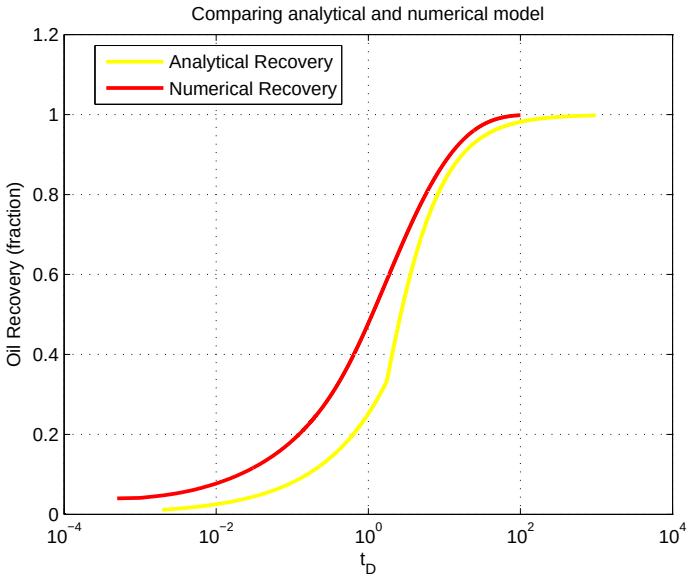

Figure 5.2.: Figure showing comparison of the analytical and numerical model.

K_{ro}^{Max}	b	J'	K_{rw}^{Max}	a	μ_r
1	1	0.19	1	1	1

Table 5.1.: Inputs for Fig. 5.2

Figure Fig. 5.2 shows a comparison of the analytical and numerical model. We see that for early times it is a poor fit, however, the numerical model in this case is run with with $K_{rw}^{Max} = 1$, which, in most cases, is not a good assumption for strongly water-wet systems. We will see what will happen if we run the simulation with a K_{rw}^{Max}-value more consistent with water-wet system in the section that follows.

5.1. Relative permeability effects:

In this section we will study the effects of changing the relative permeability parameters K_{rw}^{Max} and a.

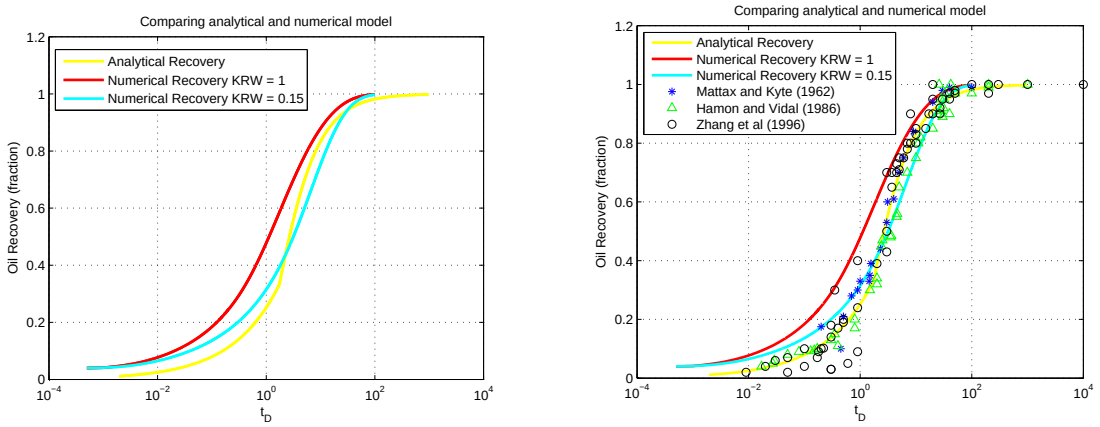

(a) Comparing the analytical model against the numerical model with different K_{rw}^{Max}-values

(b) Comparing the analytical model againt numerical model with different K_{rw}^{Max}-values, including experimental data

Figure 5.3.: Comparison of numerical and analytical model for varying values of K_{rw}^{Max}

K_{ro}^{Max}	b	$J´$	K_{rw}^{Max}	a	μ_r
1	1	0.19	0.15	1	1

Table 5.2.: Inputs for Fig. 5.3

Fig. 5.3 shows us that using a K_{rw}^{Max} value more reasonable to assume in water-wet systems gives us a much better match with both the analytical solution and experimental data.

K_{ro}^{Max}	b	$J´$	K_{rw}^{Max}	a	μ_r
1	1	0.19	1	1	1

Table 5.3.: Inputs for Fig. 5.4

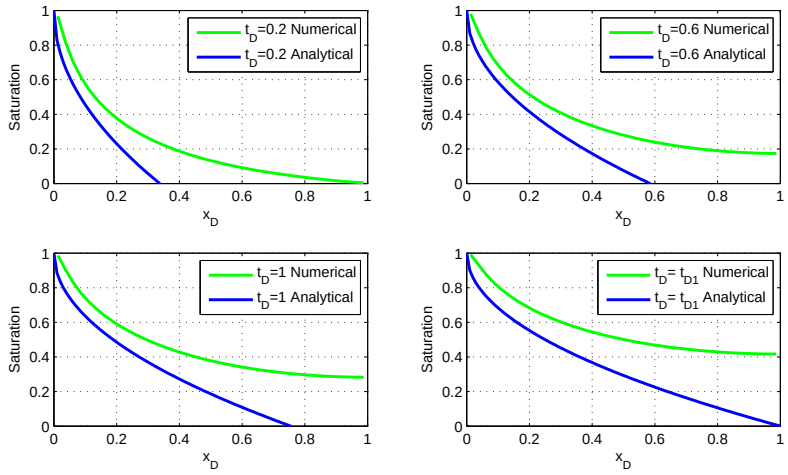

Figure 5.4.: Figure showing comparison of $S(x_D, t_D)$ between the numerical and analytical model for various early time solutions, and as listed in Tab. 5.3, $K_{rw}^{Max} = 1$

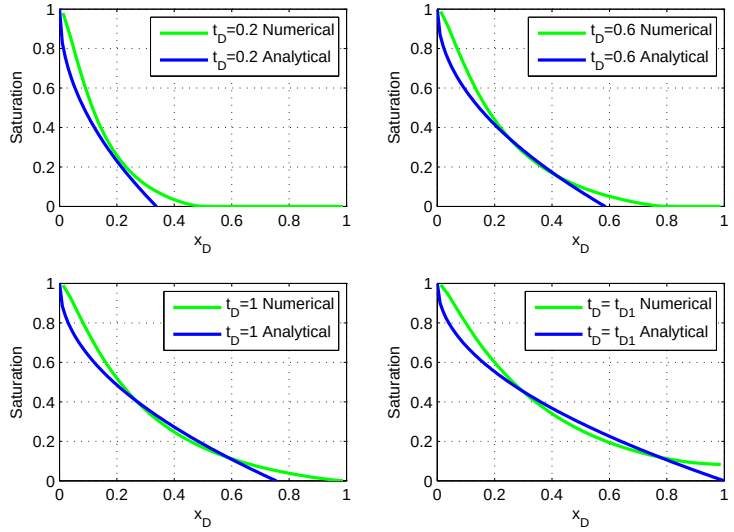

Figure 5.5.: Figure showing comparison of $S(x_D, t_D)$ between the numerical and analytical model for various early time solutions, and as listed in Tab. 5.4, $K_{rw}^{Max} = 0.15$

Fig. 5.4 and Fig. 5.5 shows $S(x_D, t_D)$ for a number of fixed times with two different K_{rw}^{Max}-values. We observe that there is a much better match in the saturation profiles between the analytical and numerical model for the value that represents a water-wet system, that is $K_{rw}^{Max} = 0.15$. We also note that the shape of the curve is slightly more convex for the numerical solution compared to the analytical.

K_{ro}^{Max}	b	J'	K_{rw}^{Max}	a	μ_r
1	1	0.19	0.15	1	1

Table 5.4.: Inputs for Fig. 5.5

Fig. 5.6 shows the numerical solution of $S(x_D, t_D = 1)$ and $\bar{S}(t_D = 1)$ for the two different K_{rw}^{Max}-values. We observe that for $t_D = 1$ the difference in recovery for the two K_{rw}^{Max}-values is just over 22%. It is thus obvious that a change in this parameter has a large impact on the solution.

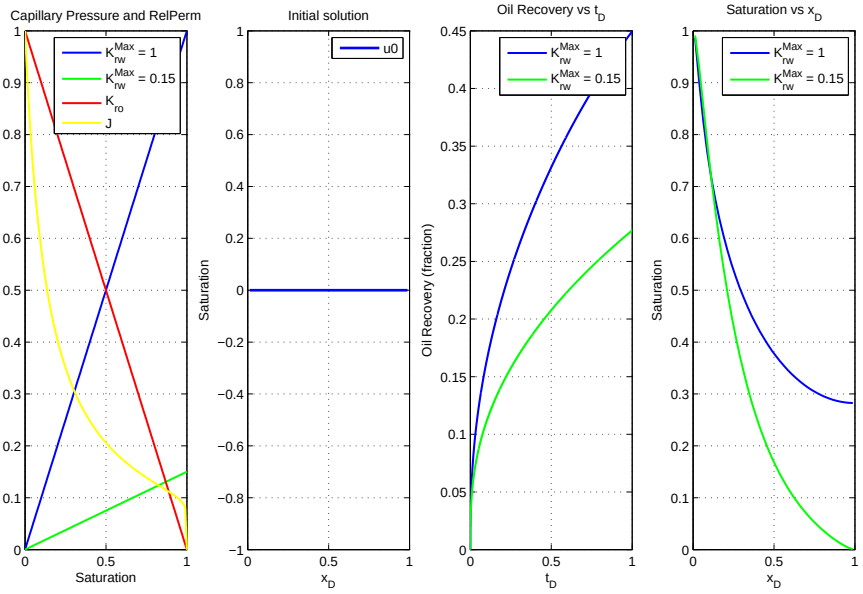

Figure 5.6.: Figure illustrating the difference in $\bar{S}(t_D = 1)$ and $S(x_D, t_D = 1)$ for two different values of K_{rw}^{Max}.

K_{ro}^{Max}	b	J'	K_{rw}^{Max}	a	μ_r
1	1	0.19	-	1	1

Table 5.5.: Inputs for Fig. 5.6

Next we will study the effects of changing the Corey water exponent, a.

K_{ro}^{Max}	b	J'	K_{rw}^{Max}	a	μ_r
1	1	0.19	0.15	-	1

Table 5.6.: Inputs for Fig. 5.7

From Fig. 5.7a we see that changing the a-value affects the shape of the relative permeability curve due to the fact that it is an exponent, referring to Eq.(2.2). We

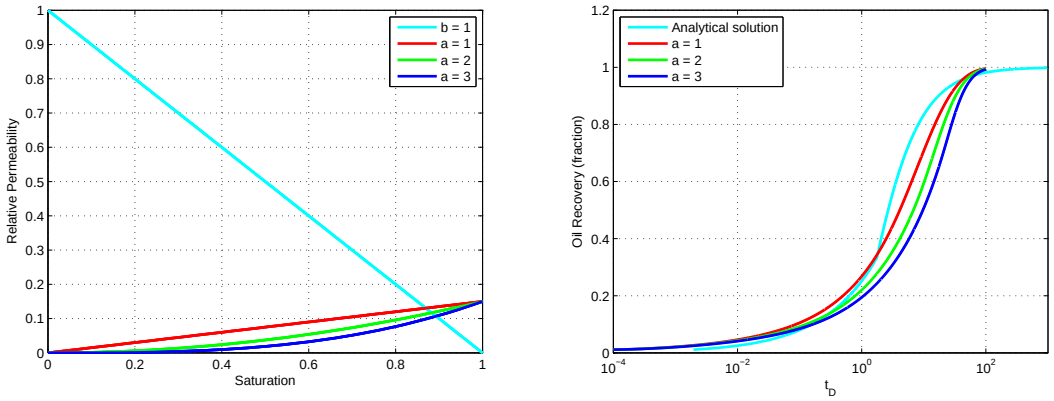

(a) Relative permeability functions for different values of the Corey water exponent, a.

(b) Oil Recovery vs dimensionless time for varying values of the Corey water exponent, a.

Figure 5.7.: Figure showing relative permeability functions and $\bar{S}(t_D)$ for varying values of a.

note that $a = 1$ gives a linear relative permeability function, the same as Tavassoli et al. [19] assumed for the Corey oil exponent. From Fig. 5.7b it can be observed that the three different a-values all give a fairly good match with the analytical solution for early times. For late times however, none of the solutions match well, but $a = 1$ gives us the best match.

When plotting $S(x, t_D)$ for fixed times in figures 5.8a and 5.8b the differences between the different a-values become clearer. We note that the saturation profiles have three distinct shapes. While $a = 1$ produces a convex profile, which is most similar to the saturation profile in the analytical solution, $a = 2$ produces a approximately linear profile, and $a = 3$ generates a concave saturation profile.

K_{ro}^{Max}	b	J'	K_{rw}^{Max}	a	μ_r
1	1	0.19	0.15	-	1

Table 5.7.: Inputs for Fig. 5.8

From Donnez [6] we find that for water-wet systems typical Corey oil exponents are in the range from 2 to 3, typical Corey water exponents are in the range 4 to 6. In Fig. 5.9 we have tested these values in the numerical simulator, using $b = 2$ and $a = 4$.

K_{ro}^{Max}	b	J'	K_{rw}^{Max}	a	μ_r
1	2	0.19	0.15	4	1

Table 5.8.: Inputs for Fig. 5.9

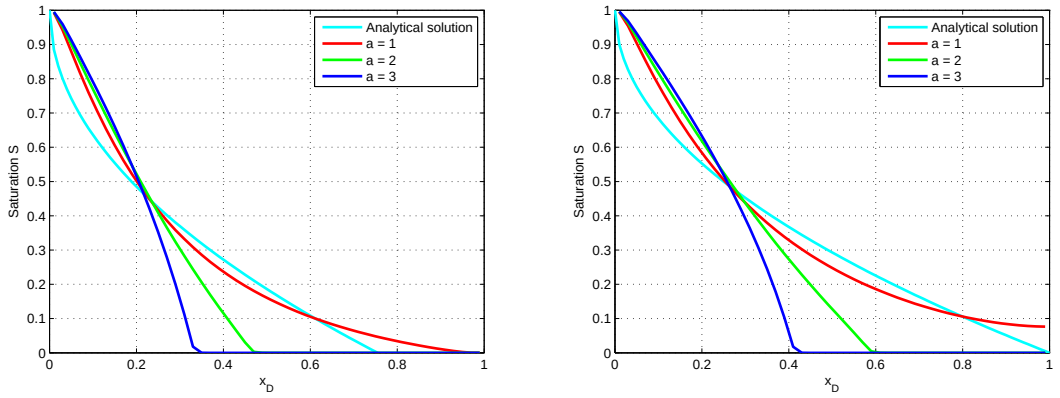

(a) Saturation profiles for different Corey water exponent, a. $t_D = 1$

(b) Saturation profiles for different Corey water exponent, a. $t_D = t_{D1} = 1.7544$

Figure 5.8.: Figure showing saturation profiles for varying values of the Corey water exponent, a, for given t_D.

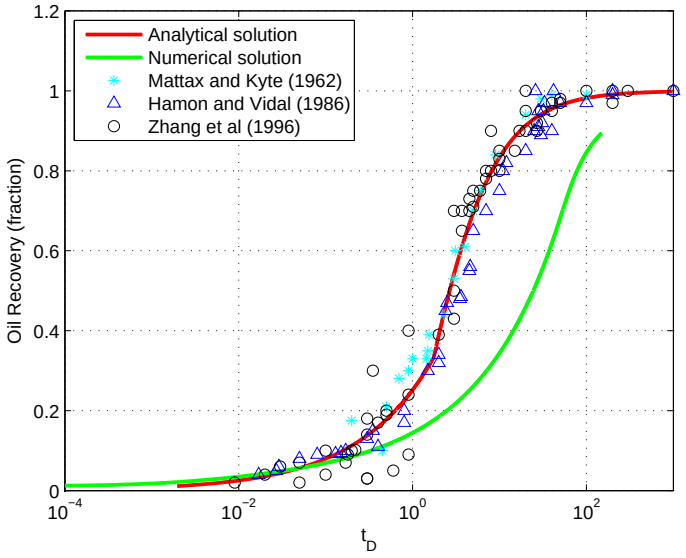

Figure 5.9.: Figure showing $\bar{S}(t_D)$ for analytical and numerical solution.

The numerical solution is run until $t_D = 150$ and is still only at 90% recovery while the analytical is close to 100%. The numerical solution in this case does not match the experimental data at all. It is worth noting that changing Corey exponential parameters to reflect, according to litterature, water-wet systems, seems to give less correlation with the analytical model. Even if we had left the Corey oil exponent equal to 1 in Fig. 5.9, we can see from Fig. 5.7 that increasing values of a shifts the numerical solution further away from the analytical solution.

5.2. Capillary pressure effects

One of the consequences of the assumptions Tavassoli et al. makes in their paper [19] is that they only consider the dimensionless capillary pressure gradient in $S = 1$, which in effect means that they ignore all capillary effects for $S \in [0, 1]$. In this section we will create different J-functions which all have a dimensionless capillary gradient of 0.19 in $S = 1$, and see how they affect our solution.

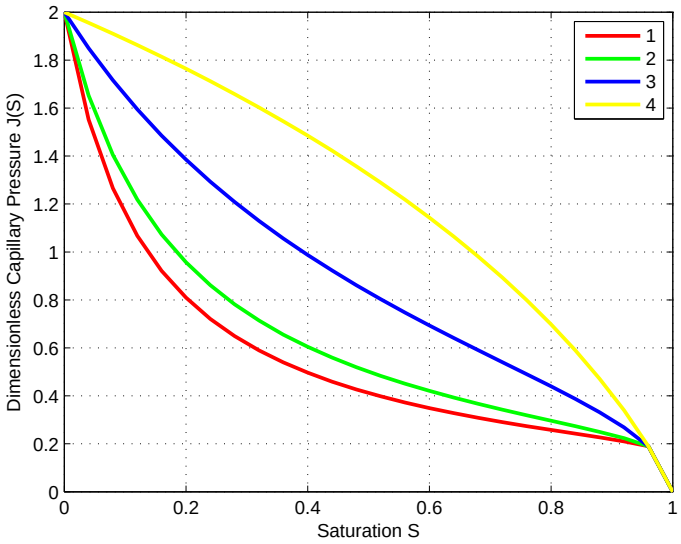

Figure 5.10.: Figure showing four different J-functions which all have a dimensionless capillary gradient, $J' = 0.19$ for $S = 1$. The LET parameter inputs can be found in Appendix A.

K_{ro}^{Max}	b	J'	K_{rw}^{Max}	a	μ_r
1	1	0.19	0.15	1	1

Table 5.9.: Inputs for Fig. 5.10

As we can see from Fig. 5.10 even though the gradient is the same in $S = 1$, using the LET-correlation we can produce capillary pressure functions that are completely

different from each other. We note that we have used capillary pressure function 1 for all numerical simulations where we haven't studied capillary pressure effects.

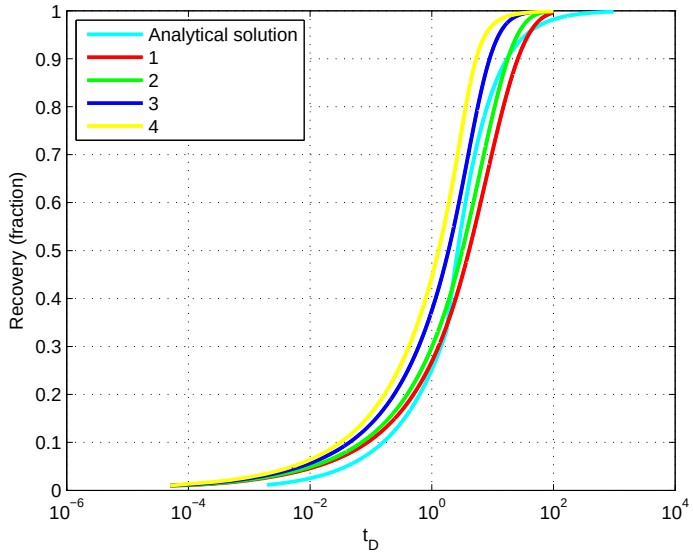

Figure 5.11.: Figure showing oil recovery vs. dimensionless time for the analytical solution and the four different J-functions shown in Fig. 5.10..

K_{ro}^{Max}	b	J'	K_{rw}^{Max}	a	μ_r
1	1	0.19	0.15	1	1

Table 5.10.: Inputs for Fig. 5.11

From Fig. 5.11 it is noticeable that the various J-functions provide us with differing recoveries for given dimensionless times. For example, J-function 4 reaches 90% recovery at $t_D = 4$ while J-function 1 doesn't reach the same recovery until $t_D = 28$. It is interesting to note that all of these different J-functions would produce exactly the same recovery in the analytical model since they all have the same value of J' for $S = 1$. However, we would have thought that such big differences in capillary pressure functions would lead to more considerable variations in the solution of the numerical model. This leads us to believe that the shape of the capillary curve does not affect the solution as much as we had expected.

K_{ro}^{Max}	b	J' analytical	K_{rw}^{Max}	a	J' numerical
1	1	0.19	see figure	1	0.19

Table 5.11.: Inputs for Fig. 5.12

As we can see from Fig. 5.12 there is a large variety in the saturation profiles for different J-functions. We see that J-function 4 has switched from a convex profile to

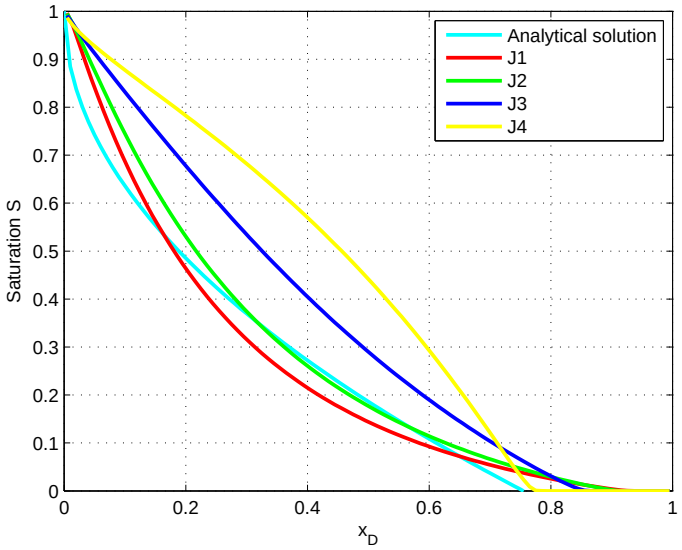

Figure 5.12.: Figure showing the difference in saturation profiles for the analytical solution and the four different J-functions shown in Fig. 5.10. $t_D = 1$.

a concave profile. As mentioned before, the recovery is the area under the saturation profile so the considerable difference in $S(x_D, t_D)$ between the various J-functions leads to the same differences we noted for the recovery.

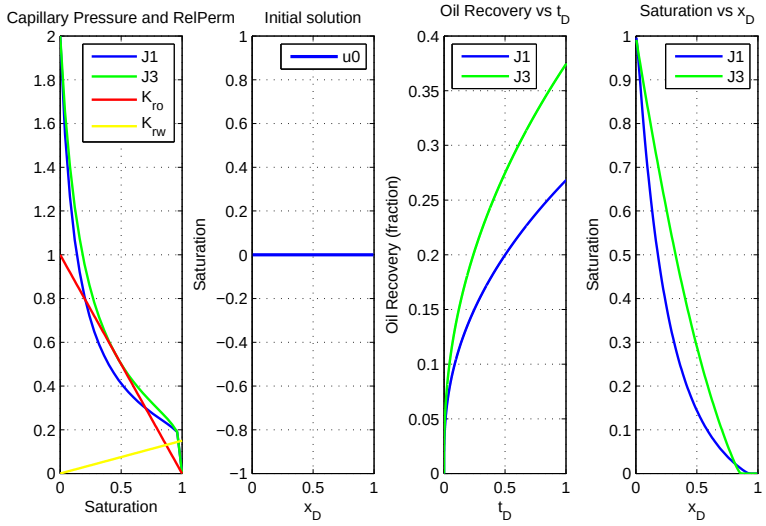

Figure 5.13.: Figure illustrating the difference in $\bar{S}(t_D = 1)$ and $S(x_D, t_D = 1)$ for J-function 1 and J-function 3 (referring to Fig. 5.10).

Fig. 5.13 depicts both $\bar{S}(t_D = 1)$ and $S(x_D, t_D = 1)$ for two of the J-functions, 1 and 3, referring to Fig. 5.10 . We observe that for $t_D = 1$ the difference in recovery is roughly 10% between the two different J-functions. We note that while

K_{ro}^{Max}	b	J'	K_{rw}^{Max}	a	μ_r
1	1	0.19	0.15	1	1

Table 5.12.: Inputs for Fig. 5.13

the saturation profile for J-function 1 is convex, J-function 3 is almost completely linear. We also note that by only using capillary pressure curves that are positive for all saturations, we have ensured that they are all for water-wet system. As we mentioned in sec. 2.4, capillary pressures for mixed-wet systems will contain both negative and positive parts depending if the surface imbibes oil or water.

5.3. Viscosity effects

At the start of this chapter we noted that the numerical model also depend on oil and water viscosity through the fractional flow term in $a(S)$, Eq.(4.2) and (4.10). To study the effects of varying viscosities it is practical to introduce a viscosity ratio $\mu_r = \frac{\mu_w}{\mu_o}$. If we introduce this relation into Eq.(4.2) we get

$$f = \frac{1}{1 + \mu_r \frac{k_{ro}}{k_{rw}}} \tag{5.1}$$

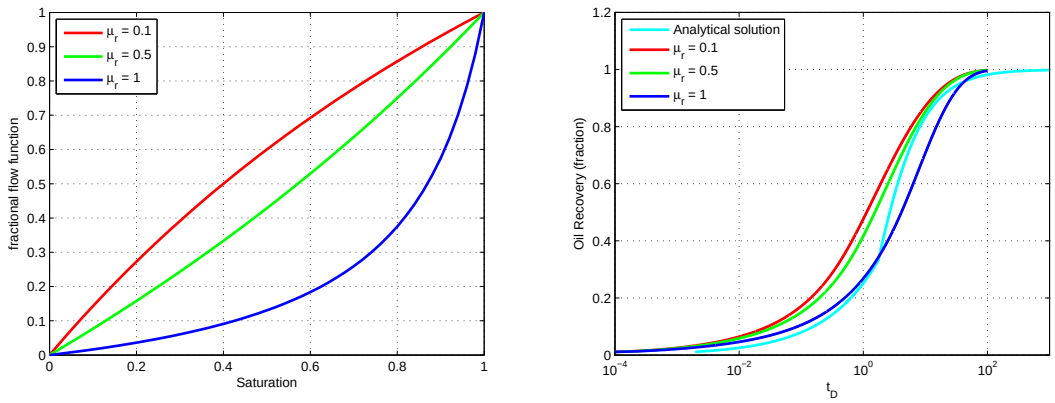

(a) Fractional flow functions for different viscosity ratios, μ_r

(b) Oil Recovery vs dimensionless time for different viscosity ratios, μ_r

Figure 5.14.: Figure showing the fractional flow functions and recovery vs. dimensionless time for different viscosity ratios.

From figure 5.14a we see that the fractional flow functions vary greatly with changing viscosity ratios. We also note that the fractional flow curves don't have the

K_{ro}^{Max}	b	J'	K_{rw}^{Max}	a	μ_r
1	1	0.19	0.15	1	-

Table 5.13.: Inputs for Fig. 5.14

characteristic S-shape. This is because we have a linear relative permeability curve for water, due to the Corey water exponent, a, beeing equal to 1. From the recovery plot in fig. 5.14b we see that for early times we have a good match with the analytical model for $\mu_r = 1$, but for late times, $\mu_r = 0.5$ and $\mu_r = 0.1$ correlates better.

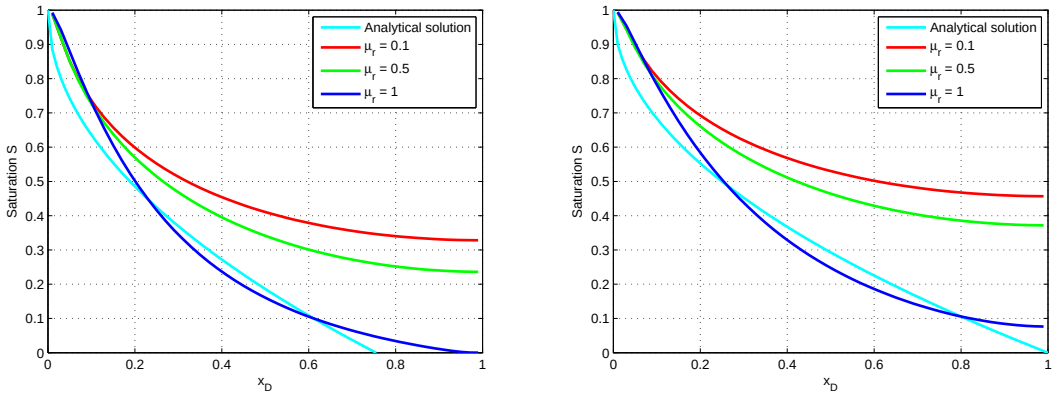

(a) Saturation profiles for different viscosity ratios, μ_r. $t_D = 1$

(b) Saturation profiles for different viscosity ratios, μ_r. $t_D = t_{D1}$

Figure 5.15.: Figure showing saturation profiles for varying viscosity ratios at given t_D.

K_{ro}^{Max}	b	J'	K_{rw}^{Max}	a	μ_r
1	1	0.19	0.15	1	-

Table 5.14.: Inputs for Fig. 5.15

When plotting $S(x_D, t_D)$ in Fig. 5.15 we see that there is considerable scatter in the saturation profiles, and for the early time solutions presented in this figure, $\mu_r = 1$ provides the closest match with the analytical solution.

It has been noted by Behbahani et al. [4] that the scatter in results for different viscosity ratios is, at least partly, due to the fact that our scaling equation, t_D does not include water viscosity. Behbahani et al. [4] also showed when plotting $\bar{S}(t)$ using the scaling equation proposed by Ma et al. [12], Eq.(2.8), produced results with considerably less scatter for different viscosity ratios. Many authors, including Tavassoli et al. [19],[4] admit that the scaling equation proposed by Ma et al. [12] which includes a geometric mean of the oil and water viscosities, provides

better matches with experimental results. Fig. 5.16 shows recovery plotted against a dimensionless time only including the oil viscosity, the same as we have used. We note that Behbahani et al. [4] have defined the viscosity ratio M as $\frac{\mu_o}{\mu_w}$ and therefore lower values of M corresponds to higher values of our viscosity ratio, μ_r. Comparing 5.14b and Fig. 5.16 we see that our results match those by Behbahani et al. [4].

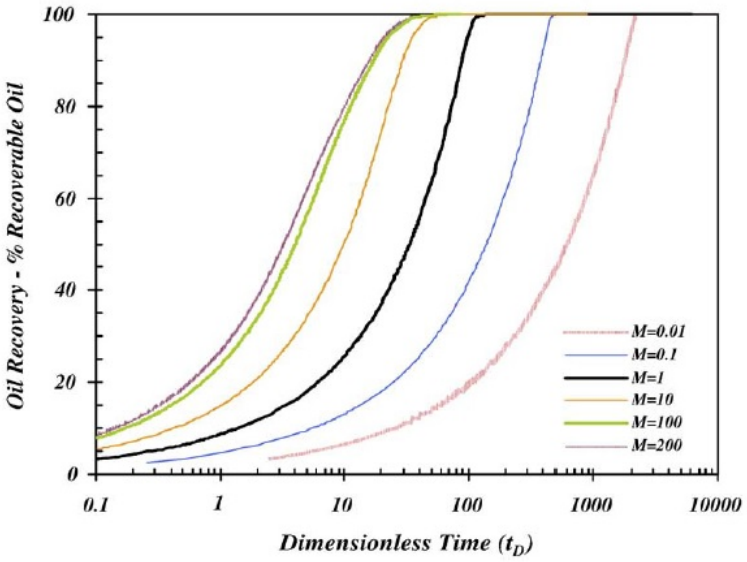

Fig. 11. Using only the oil viscosity in the definition of dimensionless time leads to a large scatter in the results from 1D simulations with different oil to water viscosity ratios, M, using network model derived data.

Figure 5.16.: Figure showing scatter in oil recoveries for different viscosity ratios. Figure from Behbahani[4]

5.4. Grid effects

As mentioned before, the analytical solution can be considered exact and stable. However, the numerical model is dependent on grid size and timestep refinement to achieve stability, referring to sec. 4.2.2. In this section will we will take a look at how altering grid size affects the solution.

K_{ro}^{Max}	b	J'	K_{rw}^{Max}	a	μ_r
1	1	0.19	0.15	1	1

Table 5.15.: Inputs for Fig. 5.17

To illustrate how different grid cell sizes(Δx) will affect our solution we run the simulation with three grid refinements. From Fig. 5.17 we can see that we have some

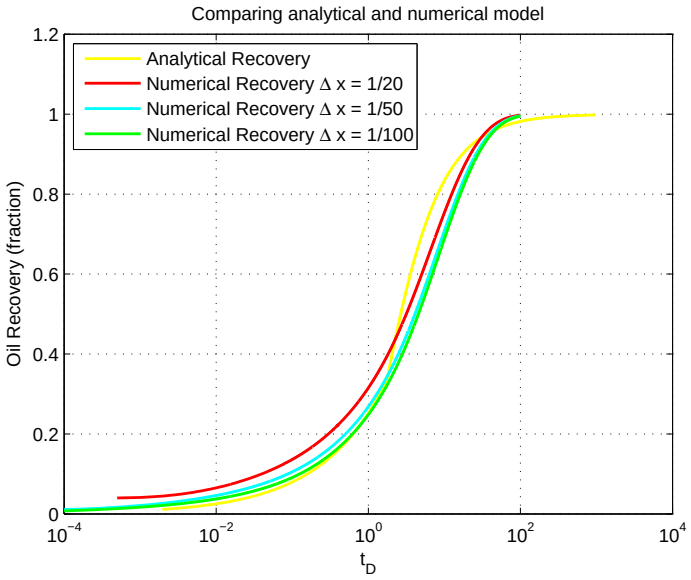

Figure 5.17.: Figure showing oil recovery vs. dimensionless time for different grid sizes, Δx.

numerical dispersion, a smearing effect, for larger grid sizes, which equals fewer grid cells. This effect of numerical dispersion would be much more noticeable if we had a sharper transition in the profile, like we would in, for example, a waterfront in a waterflood. It is noticeable that increasing the grid cells gives a more precise solution. For decreasing grid sizes, which equals more grid cells, we see that we get better fit with the analytical model, at least for early times. The effects of the grid refinements would probably be more transparent if the numerical and analytical model were a better match. These figures do however give us a good indication of how much different grid sizes affect the solution. Referring to Fig. 5.17 we note that the difference in recoveries at $t_D = 1$ is about 5% for $\Delta x = \frac{1}{20}$ and $\Delta x = \frac{1}{500}$. From Fig. 5.18 we also see that there is difference in saturation profiles between the varying grid sizes. The biggest change occurs when decreasing the grid size from $\Delta x = \frac{1}{20}$ and $\Delta x = \frac{1}{50}$.

K_{ro}^{Max}	b	J'	K_{rw}^{Max}	a	μ_r
1	1	0.19	0.15	1	1

Table 5.16.: Inputs for Fig. 5.18

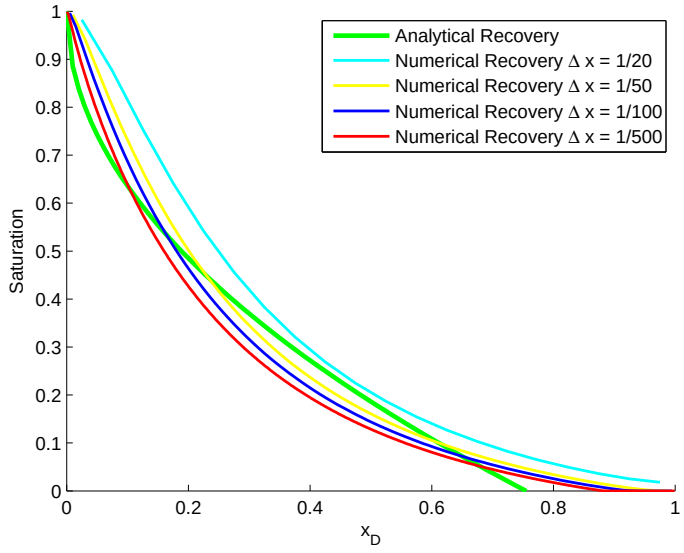

Figure 5.18.: Figure showing saturation profiles for different grid sizes, Δx.

5.5. Illustration of combined effects from capillary pressure and relative permeability.

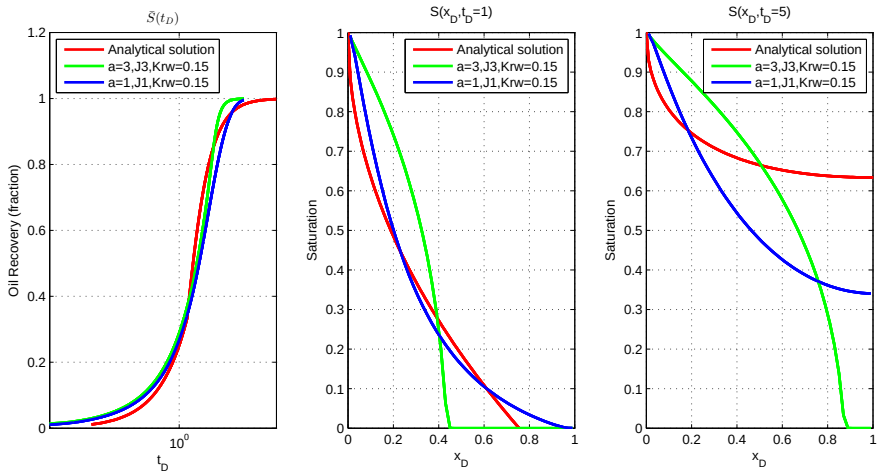

Figure 5.19.: Figure showing differences between analytical and two numerical solutions of $\bar{S}(t_D)$ and $S(x_D, t_D)$ for early ($t_D = 1$) and late ($t_D = 5$) time.

In Fig. 5.19 we have combined the effects of relative permeability and capillary effects to illustrate how much the solution can differ with changing parameters. We note that J1 and J3 in the figure corresponds to capillary pressure functions 1 and 3 from Fig. 5.10 respectively. The parameters used can all be said to be reasonable to assume in water-wet reservoirs. Although we get fairly good matches when plotting

$\bar{S}(t_D)$ it is most interesting to look at the $S(x_D, t_D)$ plots for early and late time. We see that when comparing the analytical solution with the numerical solution using $a = 1$ and J-function 1 (hereby called the convex solution), they are a good match and both have similarly shaped saturation profiles. However, when looking at the numerical solution using $a = 3$ and J-function 3 (hereby called the concave solution), we see that we get a concave saturation profile. While the analytical and convex numerical solution are closing in on the boundary, the concave numerical solution is not even halfway through the sample/reservoir. For late times this difference becomes even clearer. There is no longer a good correlation between the convex solution and the analytical solution. They do however maintain similar shapes. It is interesting to see that even after $t_D = 5$ the concave solution still hasn't reached the boundary.

6. Conclusion

In this thesis we have reproduced an analytical solution for spontaneous imbibition. When we derived the model, starting with the extended Buckley-Leverett model, we filled in many details that Tavassoli et al. [19] did not include in their paper. This should make the derivation easier to follow to someone who is less familiar with mass balance equations and spontaneous imbibition. After deriving both early- and late time solutions of the model, we plotted them as a continous function. We then observed that even though the condition that $\bar{S}(t_D)$ should be continous in the transition between the early and late time solution was fulfilled, there was a change in the gradient of the curve at the transition, which indicates that there was no continuity in $\bar{S}'(t_D)$.

When plotting $S(x_D, t_D)$ for both early and late time solutions at the transition time t_{D1}, we noticed that there was a discontinuity between the solutions. While the model was continous as a function of $\bar{S}(t_D)$, that was not the case when plotting $S(t_D)$ against the spatial variable x_D. One implication of not stating continuity in $S(x_D, t_D)$ is that for a given t_D the distribution of water in the reservoir/sample can be completely different depending on which solution one would apply.

When studying the analytical model, we tested its dependence on the three multiphase flow properties b, K_{ro}^{Max} and J' at $S = 1$. It became obvious that the Corey oil relative permeability exponent, b, had the most considerable effect on the solution. While the model has a linear dependence on K_{ro}^{Max} and J', the dependence on b is more complex, it produces changes to the gradient $\bar{S}'(t_D)$, as can be seen from Eq.(3.63) and Eq.(3.79) We noticed that even small changes in these parameters could express themselves as rather large differences in the time it would take to achieve a certain recovery and also how the water was distributed in the sample/reservoir at a given time.

There is no doubt that the analytical model provides a good fit to experimental data. Even better than we managed to produce with our numerical model. We did manage to match the analytical model for recovery and saturation profiles fairly well for early times. For late times however, we did not manage to obtain a correlation as good, and especially in the transition from early to late time solutions. While the analytical model solves this by utilizing two solutions, one for early and one for late times, our numerical solution is a single continuos function. As mentioned one of the implications of the two solutions in the analytical model are that we lose continuity in both the gradient and the saturation profile. Another reason for the analytical model to match the experimental data better than our numerical model

is most likely the scaling equation, Eq.(3.38) used by Tavassoli et al. in [19], and the fact that it does not include water viscosity.

The assumption to use the approximate solution of the weak form, the integral method, combined with the boundary condition that $\frac{\partial S}{\partial x_D}|_{x_{D=1}} = 0$, ensures that the solution is controlled by the capillary pressure and mobilities at the inlet, where S tends to 1. When we studied the capillary pressure effects however, we observed that only including the capillary gradient in $S = 1$ may be an oversimplification. We have shown that it is possible to produce notably differing results while fulfilling the condition that J' would be equal to 0.19, but still not as significant differences as we would have expected. The fact that the solution is controlled by the capillary pressure and mobilities at the inlet, where S tends to 1, is also the reason that the analytical model does not include the relative permeabilty effects for water, given by K_{rw}^{Max} and a, and in addition the viscosity of water, μ_w, from the fractional flow term. Alterations of the relative permeability parameters K_{rw}^{Max} and a can also produce highly differing results, as can alterations in the viscosity. We note that for recovery at early times the assumption in the approximate solution may not be that bad, since most of the recovery will come from areas where S is close to 1.

In conclusion we note that even though the analytical model proposed by Tavassoli et al. [19] gives good correlation with experimental data, we have proven through the numerical solution that there are dependencies that need to be evaluated and some assumptions that should be revisited. We saw that many parameters that were ignored in the model actually had a large effect on the solution. We have also shown that the model does not necessarily behave as expected for strongly water-wet media, as it claims.

In considering possibilities for further work, it would be interesting to try and incorporate more parameters in the analytical model. However, this may not be possible withouth making some alterations in the assumptions made by Tavassoli et al. [19]. If one could incorporate more parameters in the analytical model it would also be interesting to make use of another scaling group in the form of dimensionless time, t_D, to see if it would be possible to produce a solution with a better match with experimental data. Another aspect it would be useful to investigate is to see if the differential equation that we used as the basis for our numerical solution, Eq.(4.1), really is an exact solution for an imbibition process. The way we evaluated the diffusion coefficient in our numerical model is surely not the only possible method, so we are curious to see how other evaluations would affect the solution. A more detailed study with regards to how the shapes of the capillary pressure curves affects the solution would be intriguing, especially when considering that the effect of the changing shapes that we observed were less than we had expected. It would also be interesting to see if it could be possible to ensure continuity in not only $\bar{S}(t_D)$, but also in $S(x_D, t_D)$ and $\bar{S}'(t_D)$ for the analytical model.

Bibliography

[1] Abdallah.W, Buckley.J.S, Carnegie.A, Edwards.J, Herold.B, Fordham.E, Graue.A, Habashy.T, Seleznev.N, Signer.C, Hussain.H, Montaron.B, and Ziauddin.M. Fundamentals of wettability. *Oilfield Review*, 2007.

[2] Barenblatt.G.I, Entov.V.M, and Ryzhik.V.M. *Theory of Fluid Flows Through Natural Rocks*. Springer, 1990.

[3] Bear.J. *Dynamics of Fluids in Porous Media*. Dover, 1988.

[4] H.S Behbahani, G Di Donato, and Blunt. M.J. Simulation of counter current imbibition in water-wet fractured reservoirs. *Journal of Petroleum Science & Engineering*, 50:21–39, 2006.

[5] Crain.E.R. Wettability. http://www.spec2000.net/09-wettability.htm. Accessed 01.03.2014.

[6] Pierre Donnez. *Essentials of Reservoir Engineering Volume 2*. Editions Technip, 2012.

[7] Green.D.W and Willhite.G.P. *Enhanced Oil Recovery*. Society of Petroleum Engineers, 1998.

[8] Hongjing.G, Boming.Y, Yonggang.D, and Quantang.F. Fractal analysis of dimensionless capillary pressure function. *International Journal of Heat and Mass Transfer*, 69:26–33, 2013.

[9] Hundseth.Ø, Pwaga.S, Iluore.C, Perales.F, Idrees.M, and Jelmert.T. Comparative study of different eor methods. NTNU, 2010.

[10] Kleppe.H. Reservoir simulation. University of Stavanger, 2013.

[11] Lomeland.F and Ebeltoft.E. A new versatile capillary pressure correlation. In *International Symposium of the Society of Core Analysts, Abu Dhabi, UAE*, 2008.

[12] Ma.S, Morrow.N.R, and Zhang.X. Generalized scaling of spontaneous imbibition data for strongly water-wet systems. *Journal of Petroleum Science and Engineering 18*, pages 165–178, 1997.

[13] Morrow.N.R and Mason.G. Recovery of oil by spontaneous imbibition. *Curr.Opin. Colloid Interface Sci.*, pages 321–337, 2001.

[14] Schmid.K.S and Geiger.S. Universal scaling of spontaneous imbibition for water-wet systems. *Water Resources Research VOL. 48*, 2011.

[15] Schmid.K.S and Geiger.S. Universal scaling of spontaneous imbibition for arbitrary petrophysical properties: Water-wet and mixed-wet states and handy's conjecture. *Journal of Petroleum Science & Engineering*, 101:44–61, 2013.

[16] Standnes.D.C. *Enhanced oil recovery from oil-wet carbonate rock by spontaneous imbibition of aqueous surfactant solutions.* PhD thesis, University of Stavanger, 2001.

[17] Standnes.D.C. A single-parameter fit correlation for estimation of oil recovery from fractured water-wetet reservoirs. *Journal of Petroleum Science & Engineering*, 71:19–22, 2010.

[18] Standnes.D.C and Austad.T. Wettability alteration in carbonates. interaction between cationic surfactant and carboxylates as a key factor in wettability alteration from oil-wet to water-wet conditions. *Colloids and Surfaces, A: Physicochemical and Engineering Aspects*, 216:243–259, 2003.

[19] Tavassoli.Z, Zimmerman.R.W, and Blunt.M.J. Analytic analysis for oil recovery during counter-current imbibition in strongly water-wet systems. *Transport Porous Medium Vol 58*, pages 173–189, 2005.

[20] Zhang.P, Tweheyo.M, and Austad.T. Wettability alteration and improved oil recovery by spontaneous imbibition of seawater into chalk: Impact of the potential determining ions ca2+, mg2+, and so42-. *Colloids and Surfaces, A: Physicochemical and Engineering Aspects*, 301:199–208, 2007.

[21] Zhang.X, Morrow.N.R, and Ma.S. Experimental verification of a modified scaling group for spontaneous imbibition. *Society of Petroleum Engineers*, 11:280–285, 1996.

[22] Zhou.D, Jia.L, Kamath.J, and Kovscek.A.R. Scaling of counter-current imbibition processes in low permeability porous media. *Jounal of Petroleum Science and Engineering*, 33:61–74, 2002.

[23] Zolotukhin.A.B and Ursin.J-R. *Introduction to Petroleum Reservoir Engineering.* HøyskoleForlaget, 2000.

Nomenclature

A	area, L^2, m^2.
A(t), B(t)	functions of time, dimensionless.
a, b, c, f	exponents.
AFO	All-Faces-Open boundary condition.
C	integration constant, dimensionless.
J	Leverett J-function (dimensionless capillary pressure).
J'	J-function gradient at S=1.
K	Permeability, L^2, m^2 or D.
Kr	relative permeability.
L,l	length, L, m.
OEO	One-End-Open boundary condition.
Pc	capillary pressure mL^{-1},t^{-2}, Pa.
R	recovery.
S	saturation.
t	time, T, s.
TEC	Two-End-Closed boundary condition.
TEO	Two-End-Open boundary condition.
V	volume, L^3, m^3.
α, β, η, κ, γ	Dimensionless rate constants.
λ	mobility. $M^{-1}Lt$, $Pa^{-1} * s^{-1}$.
μ	Viscosity, $ML^{-1}t^{-1}$, $Pa * s$.

ϕ	porosity, dimensionless.
ρ	Density, $ML^{-3}t^{-2}$, $Kg * m^{-3}$.
σ	interfacial tension, $L^{-1}t^{-2}$, Nm^{-1}.
D	dimensionless.
i	initial.
max	maximum.
o	oil.
r	residual.
t	total.
w	water.

List of Figures

List of Tables

A. Inputs for figures

Inputs figures chapter 4:

Constant parameters for all figures in chapter 4:

- $S_{or} = 0.25$
- $S_{wi} = 0.25$
- $\emptyset = 0.24$
- K = 2554 mD = $2554 * 10^{-15}\, m^2$
- σ= 30 mNm = $30 * 10^{-3}$ N/m
- $\mu_o = \mu_w = 1$ cP = $1 * 10^{-3}\, Pa \cdot s$

Unless otherwise stated the multiphase flow parameters are also constant

- $K_{ro}^{max} = 1$
- $b = 1$
- $J' = 0.19$

LET-parameters chapter 5.

J-function 1:

- Pc_si =+100
- L_si = 0.1
- E_si = 7.194
- T_si = 1
- Pc_fi = 0
- L_fi = 10
- E_fi = 50
- T_fi = 1.2
- Pc_ref= 100

J-function 2:

- Pc_si =+100
- L_si = 0.2

- E_si = 5.212
- T_si = 1
- Pc_fi = 0
- L_fi = 1
- E_fi = 20
- T_fi = 1.2
- Pc_ref= 100

J-function 3:

- Pc_si =+100
- L_si = 0.5
- E_si = 1.985
- T_si = 1
- Pc_fi = 0
- L_fi = 1
- E_fi = 20
- T_fi = 1.2
- Pc_ref= 100

J-function 4:

- Pc_si =+100
- L_si = 0.9
- E_si = 0.5475
- T_si = 1
- Pc_fi = 0
- L_fi = 1
- E_fi = 20
- T_fi = 1.2
- Pc_ref= 100